Politecnico di Milano
Scuola di Ingegneria Industriale e dell'Informazione
Master of Science in Engineering Physics

Temperature dependent investigation of PTCDI-C_8 thin film structure

Correlatore:
Dr. Linus PITHAN

Relatore:
Prof. Giacomo Claudio GHIRINGHELLI

Studente:
Susanna BOITANO 864814

ACADEMIC YEAR 2017-2018

Alla mia famiglia,

The whole work presented in this thesis was carried out at the European Synchrotron Radiation Facility - ID03 Beamline in Grenoble, under the supervision of Linus Pithan.

Abstract

Nowadays, the fields of electronic and opto-electronic devices are basing future applications on organic semiconductors and on the study of thin film morphology made up by those materials, in order to determine and tailor the performances and the efficiency of the devices.
In particular, this thesis deals with thin films of PTCDI-C_8, a n-type organic semiconductor made up by conjugated molecule which has proven to have potential in organic opto-electronics, such as organic solar cells, and organic electronics, such as organic field effect transistors. In this case, an important parameter that influences the performances and the efficiency of the devices is the charge carrier mobility. In order to better understand how this aspect can be tailored, studies on the thin film morphology are necessary.
In the framework of this thesis an upstream study of the PTCDI-C_8 thin film morphology evolution with temperature changes will be presented. In particular the focus will be on the evolution of the crystal structure at different temperatures, analyzing the unit cell parameters and their modifications.
In the first part an introduction regarding organic semiconductors and PTCDI-C_8 will be illustrated. Then an overview of the experimental techniques and methods used to study the thin film crystal structure will be provided: X-ray techniques and organic molecular beam deposition growth method. Afterwards, the experimental results will be discussed. It has been seen that PTCDI-C_8 unit cell parameters follow a trend while changing the temperature, and at the temperature of $T \simeq 200$℃ a different crystal structure appears from grazing incident X-ray diffraction measurements.

Key words: organic semiconductors; PTCDI-C_8; unit cell parameters; crystal phase.

Sommario

Al giorno d'oggi, i settori dei dispositivi elettronici ed optoelettronici stanno sviluppando applicazioni basate su semiconduttori organici e sullo studio della morfologia dei film sottili di tali materiali al fine di determinare e modulare le prestazioni e l'efficienza dei dispositivi.
In particolare, questa tesi si occupa dello studio di film sottili di PTCDI-C_8, un semiconduttore organico di tipo n costituito da molecole coniugate che ha dimostrato di avere potenziale applicativo nell'optoelettronica organica, come le celle solari organiche, e nell'elettronica, come i transistor organici ad effetto di campo. In questo caso, un parametro importante che influenza le prestazioni e l'efficienza dei dispositivi è la mobilità dei portatori liberi di carica. Per comprendere meglio come questo aspetto possa essere sviluppato, sono necessari studi sulla morfologia del film sottile.
Nel quadro di questa tesi verrà presentato uno studio a monte dell'evoluzione della morfologia di film sottile di PTCDI-C_8 al variare della temperatura. In particolare, l'attenzione sarà focalizzata sull'evoluzione della struttura cristallina a diverse temperature, analizzando i parametri della cella unitaria e le loro modifiche.
Nella prima parte verrà illustrata un'introduzione relativa ai semiconduttori organici e al PTCDI-C_8. In seguito, verrà fornita una panoramica delle tecniche e dei metodi sperimentali utilizzati per studiare la struttura a cristalli del film sottile: tecniche a raggi X e metodo di crescita del film secondo deposito di molecole organiche. Quindi, saranno discussi i risultati sperimentali. Si è visto che i parametri della cella unitaria del film sottile di PTCDI-C_8 al variare della temperatura seguono una tendenza, e alla temperatura di $T \simeq 200$℃ appare una diversa struttura cristallina osservata attraverso misure di diffrazione con piccoli angoli di incidenza.

Parole chiave: semiconduttori organici; PTCDI-C_8; parametri cella unitaria; fase cristallina.

Contents

Chapter 1

Introduction

1.1 Organic semiconductors

The field of nanotechnology has undergone rapid progress specializing in many different branches including the investigation of organic semiconductors on a molecular length scale. Nowadays, organic semiconducting nanomaterials [1–4] are becoming increasingly significant in everyday life. But why molecular materials have to be chosen over the most common inorganic ones? Organic materials hold many distinct advantages over inorganic ones: high photon absorption and light emitting cross sections, tunability of opto-electronic properties due to the high variability of the countless numbers of molecules, biological compatibility, flexibility, since the bonding between adjacent atoms in organic molecules is governed by van-der Waals forces (Fig.1.1), an inherent compatibility with plastic substrates and amenability to low-cost and low-temperature processing methods such as melt processing, printing, and solution deposition [2, 5, 6].

These properties are at the base of new organic photo-voltaic devices (OPV) [9], organic field-effect transistors (OFETs) [10–12] and organic light-emitting diodes (OLEDs) [13–15]. The demand of lightweight and inexpensive electronic components has brought to an increased incorporation of organic materials in electronic and modern opto-electronic technological devices. Moreover, OLEDs can already be found in everyday technology such as smart-phone, smart-watch displays as well as television screens and OPV-solar cells are becoming promising thanks to new geometries such as the tandem one. The morphology of the molecular packing plays

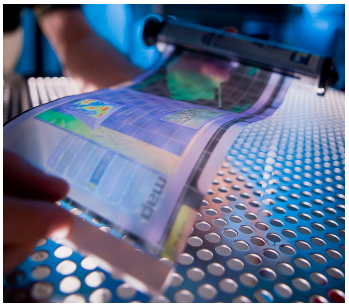

(a) Flexible display [7].

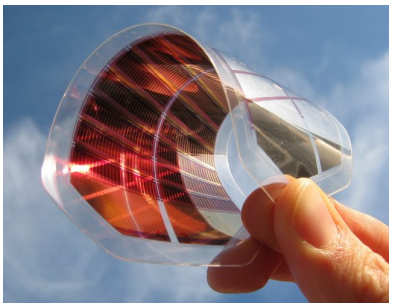

(b) Flexible OPV solar cell [8].

Figure 1.1: Examples of opto-electronic devices.

a crucial role in the performance of the molecular organic devices [16–18]. In order to reach high performances for these optical and electrical characteristics, growth, structure and morphology of the organic semiconducting materials need to be tailored. Different devices face different needs for an optimum performance. OFETs require high charge carrier mobility and in OPVs the architecture and structure at the organic/organic interface play a crucial role. The charge carrier mobility issue is one of the major problems of organic semiconductors. In fact, in thin film geometry, the charge carrier mobility of an OFET strongly depends on the structural order of the organic semiconducting film and on the morphology and structure of the first organic layers at the organic/inorganic interface. Optimum charge carrier transport occurs when the inter-molecular overlap of electronic π-orbitals of adjacent molecules is maximized. This behaviour can be found in single crystalline films. Considering the structure at the organic/organic interface in OPVs, a large interfacial area between p- and n-type material is provided to create and harvest as many excitons (electron-hole pairs) as possible. Organic semiconductors are materials based on carbon-containing

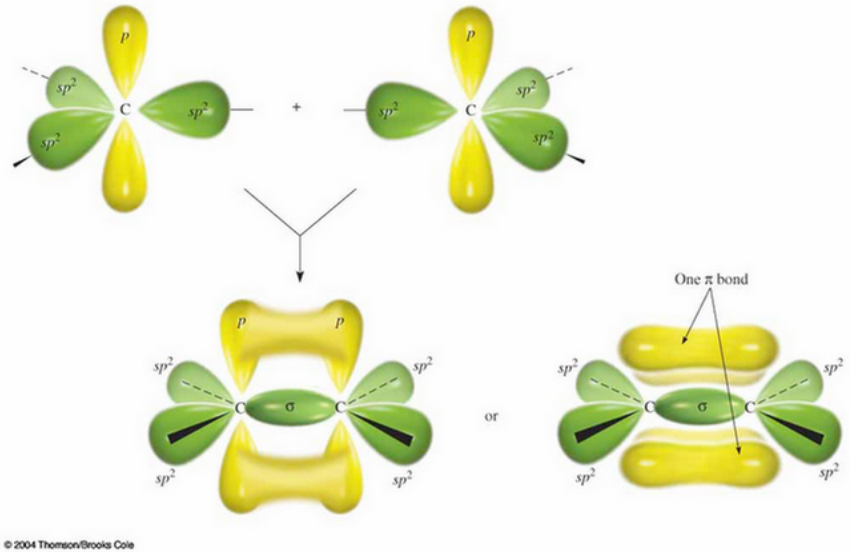

Figure 1.2: Two sp2 hybridized carbons are forming a σ-bond (yellow) and a π-bond (green) [19].

molecules. Their semiconducting properties are attributed to the conjugated π-electron systems, consequence of sp2 hybridization of the carbon atoms, in their skeletal structures. In Fig.1.2 two sp2 hybridized carbon atoms are illustrated. The two atoms form two types of bonds: the center bond (green) is a σ-bond made up by orbitals overlapping on the C-C axis; the two p_z orbitals (yellow) form the π-bond, made up by orbitals overlapping laterally, defining two regions opposite with respect to the nodal plane.

Because of the conjugated π-electron system, the electrons result delocalized on the molecule. This delocalization is responsible for the opto-electronic properties of organic semiconductors. In fact, as the molecules are more close together, the π-conjugated orbitals create bigger region in which electrons are delocalized [20], leading to a higher two-dimensional charge transport, and so a higher electron and hole mobility [21, 22]. There are two possible stacking configurations: the vertical and the horizontal one (Fig.1.3). As it is clear from the π-system that arises from each configuration, with the horizontal stacking (1.3a), typical of flat-lying molecules, the p_z-orbitals are horizontally oriented and their overlap creates vertical regions in which the electrons are delocalized, so the charge transport is vertical. Differently, for the vertical stacking (1.3b),

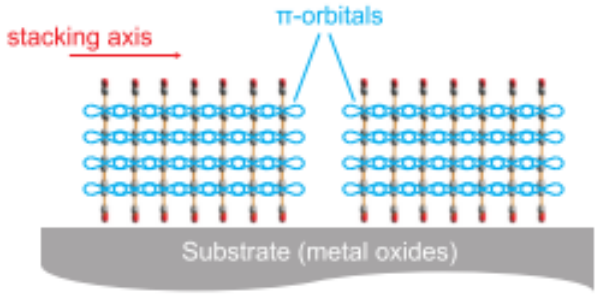

(a) Horizontal stacking: the p_z orbitals overlap vertically

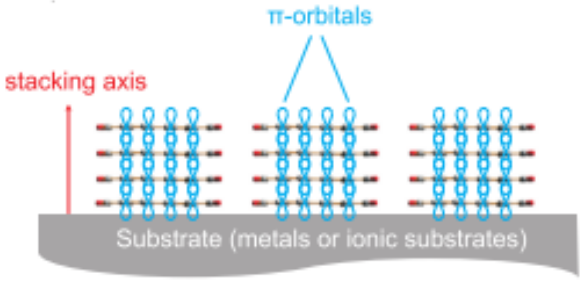

(b) Vertical stacking: the p_z orbitals overlap horizontally: two-dimesional charge transport

Figure 1.3: Horizontal and vertical stacking geometry with the corresponding π-systems that dominate the electronic transport [23].

typical of upright-standing molecules, the p_z-orbitals are vertically oriented and the region in which electrons are delocalized extends horizontally leading to the two-dimensional charge transport that can extend for larger areas.

However, for organic semiconductors mobility $\mu < 1\text{cm}^2/V \cdot s$ is still not comparable (by several orders of magnitude) to the one of inorganic materials, for crystalline silicon $\mu \simeq 1400\ \text{cm}^2/V \cdot s$ and for polycrystalline silicon $\mu \simeq 100\ \text{cm}^2/V \cdot s$ [24]. For this reason, progresses in the organic electronic field are based on the study of materials with higher charge carrier mobility, which relies on the ability to grow organic films with the highest crystallinity and the lowest defect concentration. This peculiar challenge allows to design functional molecular materials [3] exploiting their anisotropic properties related to the organic molecules that, in turn, define the

anisotropic properties of the organic films on the macroscopic scale. So, the determination of the molecular packing and of the molecular orientation of organic semiconductor is an important point in the thin-film geometry and moreover it is a crucial part for modelling the band structure on which the charge-carrier properties depend [25]. In fact, the more the molecule will have vertically aligned p_z orbitals, the higher will be the area covered by two-dimensional charge transport.

1.2 PTCDI-C8

Organic materials can be divided in two main groups depending on the size of their functional group: polymers and low-weight molecules. Organic polymers are characterized by higher solubility which makes them suitable for solution deposition [26], in fact they are mainly used in low-cost ink-jet printing of electrical circuits and displays [27]. Low-weight organic molecules, on the other hand, can form highly ordered crystalline structures with better electrical transport properties [21, 28, 29]. In this thesis the low-weight organic n-type semiconductor N,N'-dioctyl-3,4:9,10-perylene tetracarboxylic diimide (PTCDI-C_8) will be studied. PTCDI-C_8 is an organic semiconductor with a planar perylene core in the centre and two alkyl side chains. In recent years perylene diimides have been identified as one of the few promising n-type organic semiconductors with reasonable charge carrier mobilities [30–32]. PTCDI-C_8 chemical formula is $C_{40}H_{42}O_4N_2$ (Fig.1.4a) and the molecular representation is illustrated in Fig.1.4b.

PTCDI-C_8 charge carrier mobility can reach values up to $\mu \simeq$

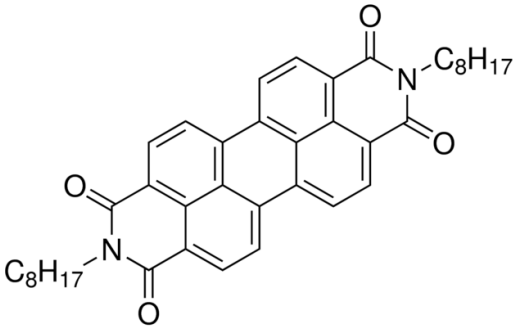

(a) Chemical structure.

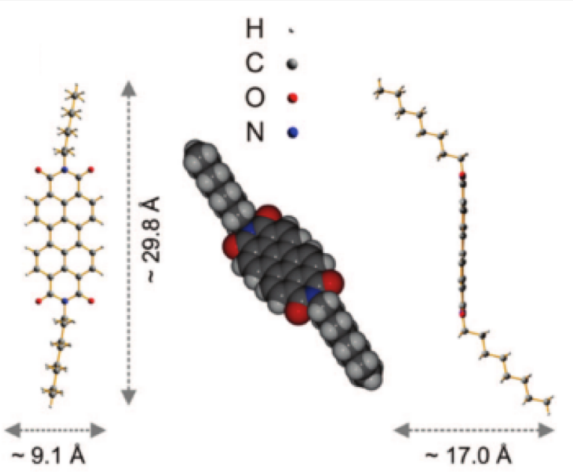

(b) Dimensions [25]

Figure 1.4: Chemical and molecular structure of PTCDI-C_8.

$1.7 cm^2/Vs$ with adequate growth temperatures [33, 34] and nowadays it is largely used in OFETs [35, 36] and OPV devices [32] [37]. It is known that the morphology of self-assembled perylene diimide structures, which gives such a promising charge carrier mobility, largely depends on the nature of the side chains. Substituted perylenes are also technologically relevant, the most prominent ones are perylene- 3,4-9,10-tetracarboxylic dianhydride (PTCDA) and N,N'-substituted perylene-3,4-9,10-tetra- carboxylic diimides (PTCDIs) [38]. The alkyl side chains of PTCDI-C_8 lead to hydrophobicity as well as electronic interferences into the self-assembly process [39], helping the molecules to get more precise alignment relative to each other [40]. To better understand this high carrier mobility it is important to study the morphology of the molecules in the thin film. Molecular thin films can grow up with amorphous or crystalline nature depending on the ambient conditions during growth [3]: PTCDI-C_8 molecules are packed in a slipped co-facial alignment with the π-π stacking along the b-axis [41] as shown in Fig.1.5, and they grow in a crystalline fashion even on amorphous materials, such as silicon dioxide and aluminum dioxide.

Moreover, PTCDI-C_8 thin films show a strong temperature dependence, affecting consequently their optical properties [42]. For these motivations, in the framework of this thesis the study of the evolution of the PTCDI-C_8 crystal structure with temperature variation has been carried out.

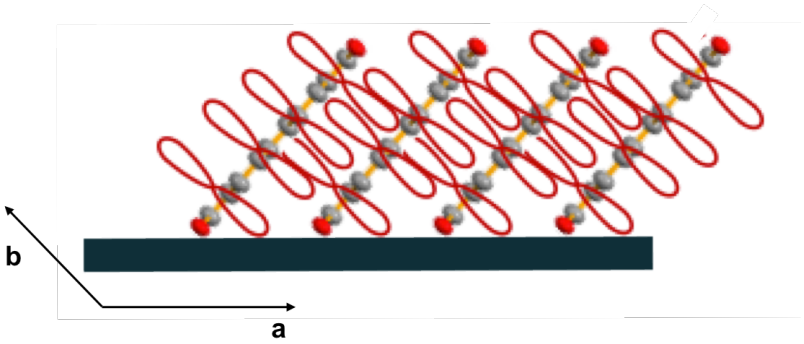

Figure 1.5: Schematic view of PTCDI-C_8 stacking. The p_z-orbirals are overlapping along the b-axis.

Chapter 2

Experimental Techniques and Methods

In the following chapter the experimental facility in which the experiment has been performed is described. First the European Synchrotron Radiation Facility is presented. Afterwards, the ID-03 beamline and the experimental setup used are illustrated. Then X-ray scattering techniques in the framework of this thesis are introduced. Finally, organic molecular beam deposition is explained.

2.1 Experimental facility

2.1.1 The European synchrotron radiation facility

The work presented in this thesis has been entirely performed at the European Synchrotron Radiation Facility (ESRF) in Grenoble (France). The ESRF is a joint research facility supported by 22 countries, it is operating since 1992 and it is one of the most powerful third generation synchrotron sources worldwide. In particular, the ESRF is one on the most important third generation synchrotrons and in 2020 it will be upgraded to Extreme Brilliant Source [43].

The ESRF is an extremely powerful source of X-rays of high energy, "hard" X-rays, which have wavelengths of $\lambda = 0.10$ nm to $\lambda = 0.01$ nm or energies in the range $E = 10$ kev to $E = 120$ keV. Synchrotron science depends on one physical phenomenon: when a moving electron changes direction, it emits energy. Precisely, when the electron is moving fast enough, the emitted energy is at X-ray

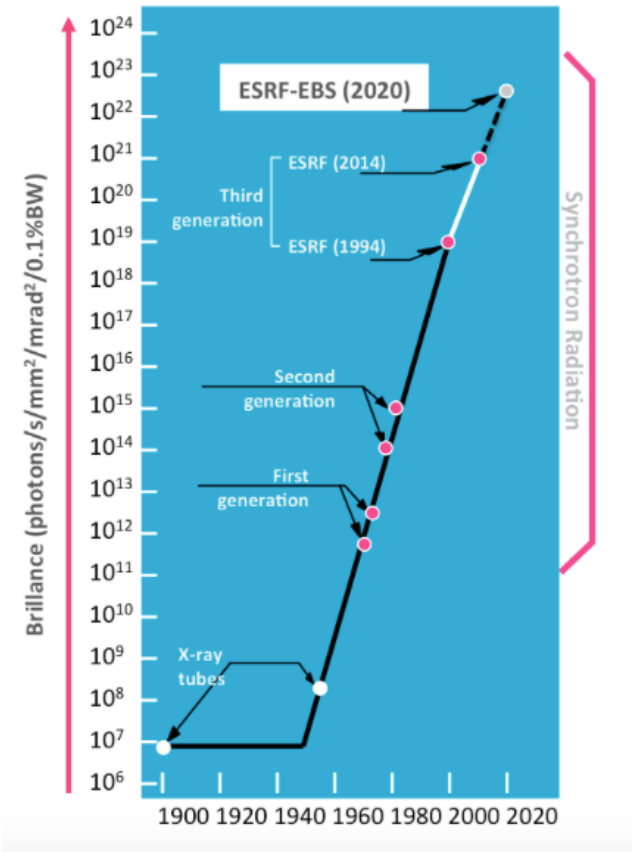

Figure 2.1: Plot of the brilliance evolution in the last century and in the future years. It is possible to distinguish the first, second and third generation of synchrotron.

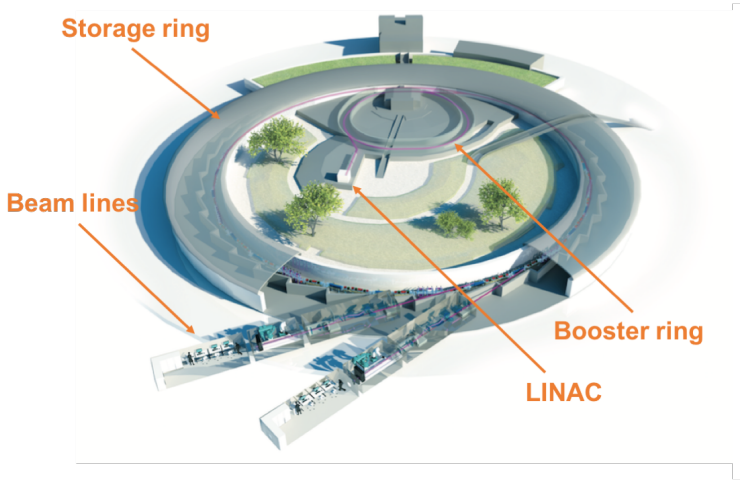

Figure 2.2: Schematic illustration of the ESRF facility [44].

wavelength. The working principle of a synchrotron is to accelerate the electrons in order to reach high energies, and make them change direction periodically. The resulting X-rays are emitted as dozens of thin beams, each one directed toward a beamline next to the accelerator. In Fig.2.2 the main components of the ESRF are shown. The electrons, generated by electron gun, are initially accelerated up to 200 MeV by linear electric field (LINAC) at the center of the whole ring. Once the electrons have reached that energy, they are injected in the Booster-Synchrotron.

The Booster-Synchrotron is an electron accelerator of 300 m long pre-accelerator, where electrons travel reaching their final energy of 6 GeV. Then, from the Booster-Synchrotron the electrons are finally injected into the storage ring in which they travel as bunches. Bunches are packages of different numbers of electrons them depending on the filling mode set. The lower is the number of electrons bunches, the higher is the current, and the power, for each bunch. The storage ring is a tube kept under ultra-high vacuum (UHV) up to P=10^{-11} mbar, 844 meter-long, surrounded by an array of magnets that focus and bend the beam, separated by straight linear sections. Once in the storage ring, electrons have a lifetime about 60h and can emit radiation. Travelling electrons loose energy when emitting radiation, so in order to maintain electrons' high energy, radio frequency cavities are present both in the Booster and in the Storage ring. These cavities are conductive metal structures which reshape the modes of oscillation of the electromagnetic field in order

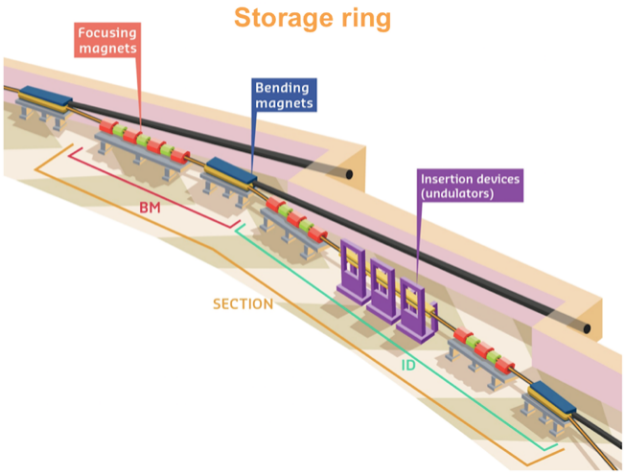

Figure 2.3: Storage ring section showing the two king of X-ray sources: bending magnets and insertion devices [44].

to have a component parallel to the electrons motion. The cavities' oscillation frequencies are controlled by a radio frequency system, set to 3 GHz (35 MW power) for the booster ring and at 352 MHz (9 MW power) for the storage ring. The radio frequency cavities control the filling mode of the ring. In fact, the maximum number of bunches in the ring is given by the length of the ring divided by the radio frequency and is achieved with the uniform filling mode. When electrons are forced to travel in curved paths they loose part of their kinetic energy, which is converted in emitted radiation (law of conservation of energy): the Bremsstrahlung radiation. Then, the beam can be tailored: trough bending magnets or through insertion devices (Fig.2.3).

Bending magnets are placed in particular positions in the storage ring after the straight sections in order to deflect electrons path. They generate a magnetic field which makes the electron trajectories curve. After travelling through the bending magnets, electrons emit X-ray radiation tangent to the beam axis (Fig.2.4a), covering a wide and continuous spectrum [45]. On the other hand, the insertion devices are placed in the straight section between the bending magnets. These magnetic structures are made up of a complex array of small magnets which force the electrons to follow an undulating, or wavy, trajectory. In this way, the radiation emitted at each consecutive band overlaps and interferes with that from the other bands. This mechanism, shown in Fig.2.4b leads to the generation

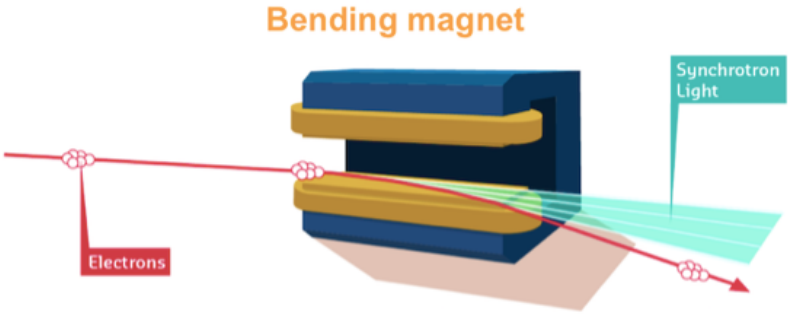

(a) Bending magnet

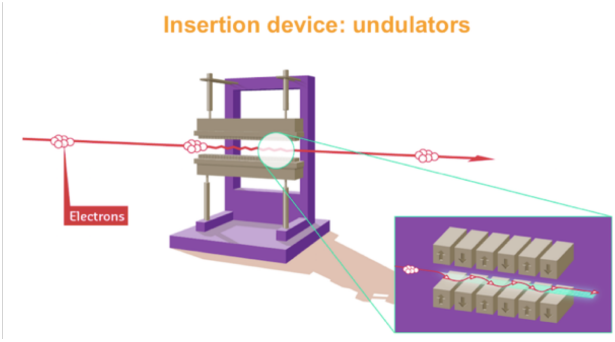

(b) Insertion device

Figure 2.4: Bending magnet (a) and insertion device (b) illustrations at ESRF [44].

of a much more brilliant beam of radiation with respect to the one produced by a single magnet.

2.1.2 ID-03 surface diffraction beam-line

ID-03 is an ESRF undulator beam-line dedicated to surfaces and interfaces structural characterizations through Surface X-Ray Diffraction (SXRD). The photon energy is continuously tuneable, giving a flux exceeding 10^{12} ph/s in the whole 5-24 keV energy range. SXRD is a well established technique to study surfaces and interfaces [46]. The research topics developed at ID-03 varies from surface crystallography in UHV to atmospheric pressure, in-situ characterization of dynamical phenomena to catalysis and electrochemistry. The experimental techniques available at the beam-line are surface X-ray diffraction (XRD), grazing incidence small angle X-ray scattering (GISAXS), X-ray diffraction (XRD) and coherent diffraction imag-

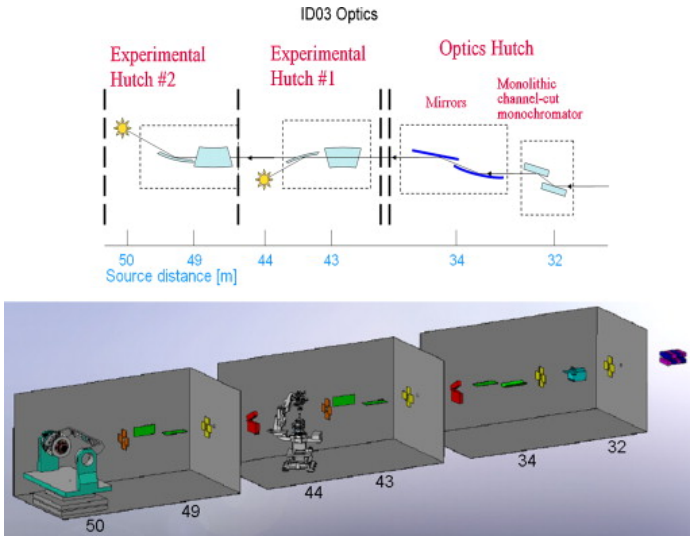

Figure 2.5: A schematic view of the optical elements at the ID03 beamline. The numbers below the graph are the distance to the undulators (middle of the straight section) [47].

ing. In Fig.2.5 schematic view of the layout of the beam-line is presented. Three main components are present: the optical hutch and two experimental hutches, the experimental hutch 1 (EH1) and the experimental hutch 2 (EH2).

In the optics hutch there are the optical elements which the beam encounters along his path: channel cut monochromator, cylindrical bendable mirror, second mirror; in the first experimental hutch: vertical focusing KB mirror, horizontal focusing KB mirror, sample; in the second experimental hutch: vertical focusing KB mirror, horizontal focusing KB mirror, sample.

The first hutch contains a vertical geometry diffractometer that can accommodate small chambers (UHV equipment, electrochemical cells, etc) on the hexapod present at the sample position. The second hutch is housing a horizontal geometry z-axis diffractometer with a UHV chamber (main chamber) for in-situ surface preparation and growth, surface magneto-optic Kerr effect (SMOKE) and Auger Electron Spectroscopy (AES). The UHV conditions are guaranteed by turbo-molecular and titanium sublimation pumps [48].

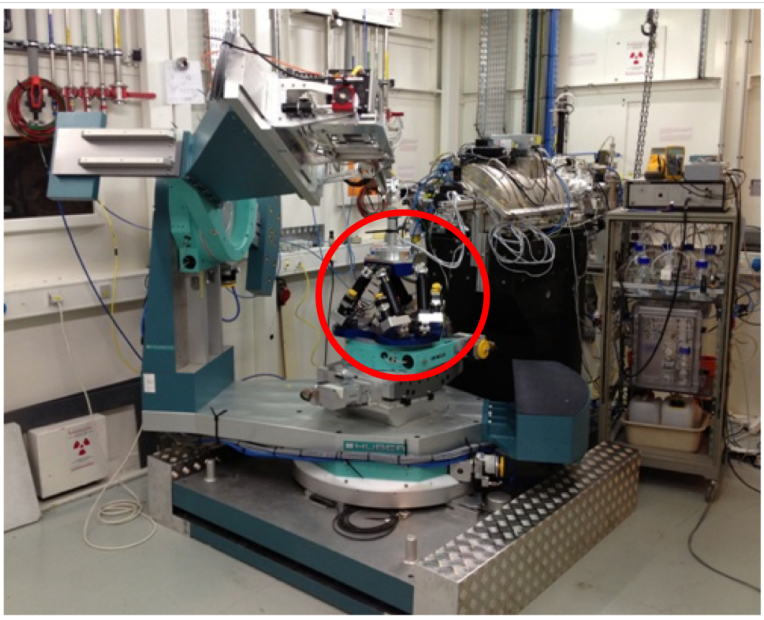

(a) EH1

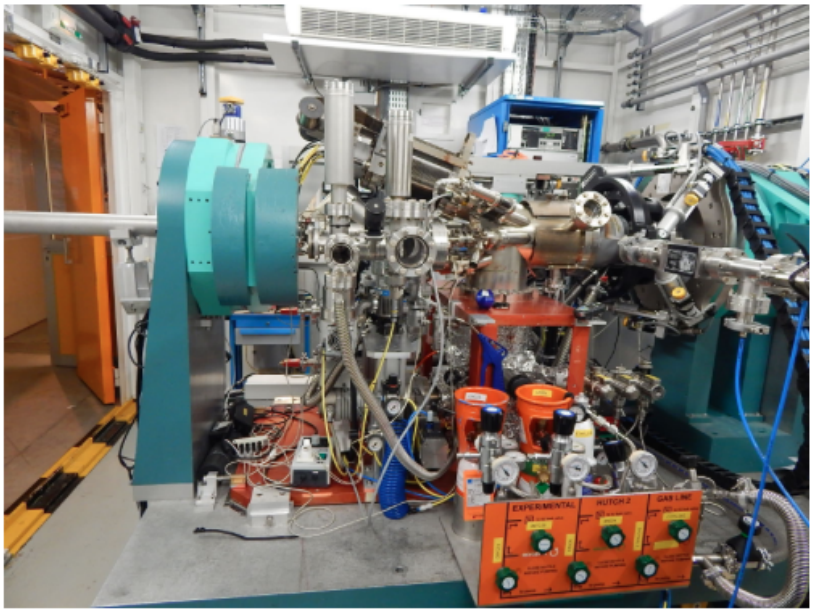

(b) EH2

Figure 2.6: Photos of the two diffractometers at ID-03 beam-line [48]. In (a) the hexapod is highlighted in the red circle.

2.2 Experimental setup

The experiment illustrated in this thesis has been performed using the diffractometer present in the experimental hutch 1 of ID-03 beam-line. In Fig.2.7 the focus of the experimental setup is shown. The experiment has been performed in UHV conditions in order to reduce as much as possible air X-ray scattering arising from air, using a portable UHV chamber which has been mounted on the hexapod at the center of the EH1 diffractometer. The hexapod allows translations and rotations along the three directions *x, y, z*. The UHV chamber is belted by a Beryllium window which allows the X-ray access, in fact Beryllium has small atoms (small electronic core) and low density and thus absorbs relatively few X-rays as opposed to other materials, this characteristic makes Beryllium suitable for maximum flux transmission. X-rays, simplified by the yellow dashed line in Fig.2.7, were impinging from the right, passing through the beryllium window and hitting the sample. The diffracted or reflected beam was then detected by the large area detector Pilatus 300K. In front of the detector an apparatus was mounted in order to clean the incoming radiation from all those scattering component arising from outside the sample.

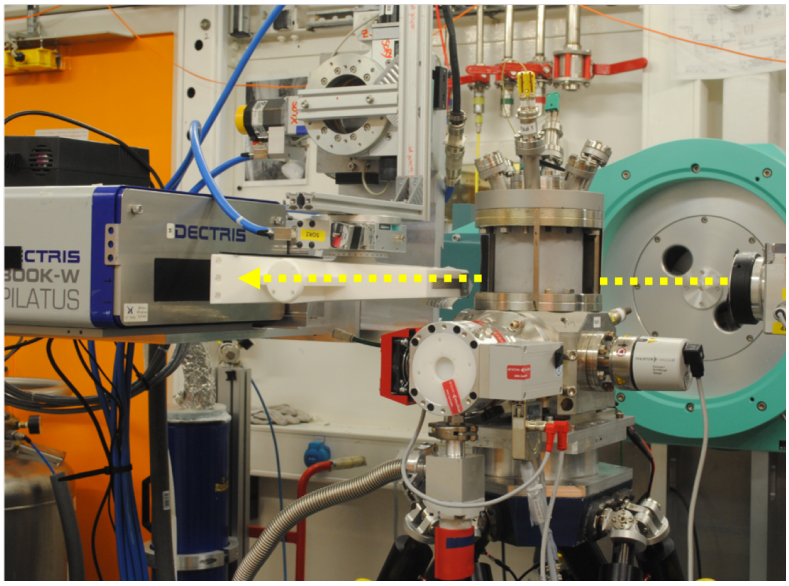

Figure 2.7: Experimental setup adopted for the experiment.

2.3 X-ray scattering

X-ray scattering is a powerful tool to explore the crystal structure, chemical composition, and structural and physical properties of materials and thin films with high temporal and spatial resolution [49, 50]. Moreover, X-ray scattering methods allow accessing a variety of thin film properties and enable non-invasive in situ and real time measurements. X-rays are an electro-magnetic radiation with wavelength in the range $0.01-10$ nm which can be described by a linearly polarized, plane wave $\mathbf{E}(\mathbf{r},t)$:

$$\mathbf{E}(\mathbf{r},t) = \hat{\epsilon}\mathbf{E}_0 exp(i\mathbf{k}\cdot\mathbf{r} - \omega t) \tag{2.1}$$

where $\hat{\epsilon}$ is the polarization vector, $\mathbf{k}$ is the wave vector along the direction of propagation and since electro-magnetic waves are transverse waves $\hat{\epsilon}\cdot\mathbf{k} = 0$, and $\mathbf{k}\cdot\mathbf{E} = \mathbf{k}\cdot\mathbf{H} = \mathbf{0}$ where **E, H** are the electric and the magnetic field respectively. The numerical relation between the wavelength and the photon energy is:

$$\lambda[\text{nm}] = \frac{hc}{E} = \frac{1239.8}{E[eV]} \tag{2.2}$$

One X-ray photon can interact with an atom in one of two ways: it can be scattered or it can be absorbed. In this section the scattering process will be described. Referring to the classical description

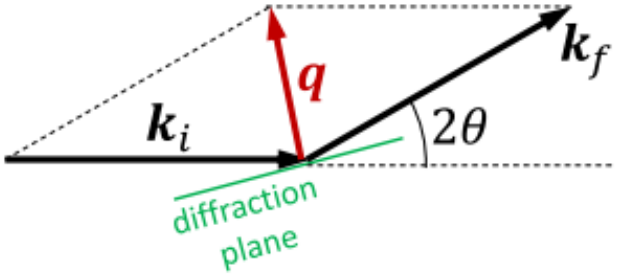

Figure 2.8: Illustration of the momenta involved during elastic scattering.

of the scattering event, the electric field of the incident X-ray applies a force on the electronic charge, which is accelerated and radiates the scattered wave. The scattering can be *elastic*, where the kinetic energy of a particle is conserved in the center-of-mass frame, or *inelastic*, known as Compton effect, where the energy is not conserved anymore. In the following, scattering will be assumed to be elastic: $\mathbf{k_i} = \mathbf{k_f}$, where $\mathbf{k_i}, \mathbf{k_f}$ are the incident and scattered wave vector respectively. The results which are arising from scattering experiments are maps in the momentum space where on the x-axis there is the transfer momentum and on the y-axis the scattered intensity. The transfer momentum $\mathbf{q}$, depicted in Fig.2.8, is defined as follow:

$$|\mathbf{q}| = 2|\mathbf{k}| \sin\theta \tag{2.3}$$

where $\mathbf{q} = k_i - k_f$ and 2θ is the experimental scattering angle.

Within the framework of crystalline materials the incident X-ray beam gets scattered at the periodic planes of the crystalline sample. This phenomenon is described by the Bragg's law which sets the condition for constructive interference for the electromagnetic waves:

$$m\lambda = 2d \sin\theta \tag{2.4}$$

where m is an integer, d is the distance between two lattice planes, θ and is the incidence angle. In scattering experiments the transfer vector $\mathbf{q}$ is present in its two directions: the one normal to the sample surface, labelled as $\mathbf{q}_\perp$ and the in-plane, denoted as $\mathbf{q}_\parallel$. So, depending on the scattering experiment, it is possible to probe

the scattering intensity towards the sample's in-plane or out-of-plane directions to get different properties of the crystal structure.

2.4 X-ray reflectivity

X-ray reflectivity (XRR) is a is a surface-sensitive analytic technique, a powerful tool to probe the structural properties of thin films. At certain specific wavelengths and incidence angles, crystalline materials produced intense peaks of reflected radiation. The basic idea of XRR technique is to reflect X-ray beam from a flat surface and to then measure the intensity of X-rays reflected in the specular direction. Using the Parratt algorithm the electron density profile within the crystal can be extracted [51]. When dealing with XRR the following conditions are fulfilled: elastic scattering of the incident wave ($\mathbf{k_i} = \mathbf{k_f} = 2\pi/\lambda$); specular X-ray reflection ($\theta_i = \theta_f$). Consequently, the transfer momentum, or scattering vector $\mathbf{q}$ presents only its component perpendicular to the surface and XRR measurements are displayed as a function of the length of the scattering vector $|\mathbf{q}_\perp|$, which can be expressed as a function of the wavelength λ and the scattering angle θ:

$$|\mathbf{q}_\perp| = \frac{4\pi}{\lambda} \sin\theta \tag{2.5}$$

In Fig.2.9 an example of XRR pattern is depicted.

First of all, the position of the critical edge gives information on the electron density $\rho_e l$ of the material at the interface. For $\mathbf{q}_\perp > \mathbf{q}_c$ a fast decay of the reflectivity R is observed, where $\mathbf{q_c}$ is the critical scattering vector below which total external reflection, and thus a constant reflectivity of almost 100%, occurs. A dependence of R on $\mathbf{q}$ can be extracted From the Fresnel equations, obtaining $R \propto \mathbf{q}_\perp^{\mathbf{4}}$. Then, for low scattering angles information about the total film thickness and smoothness can be recovered. The constructive and destructive interference of the X-rays reflected at the vacuum/film interface and at the film/substrate interface leads to the appearance of periodic oscillations, also called Kiessig fringes. For a rough thin film less X-rays are reflected specularly but also diffusely. This result is reflected in the shape of the fringes which are smeared out and the number of fringes decreases when increasing the surface roughness. From the period of these oscillations $\Delta\mathbf{q}\perp$ (distance between two consecutive minima) the thickness of the thin film D can

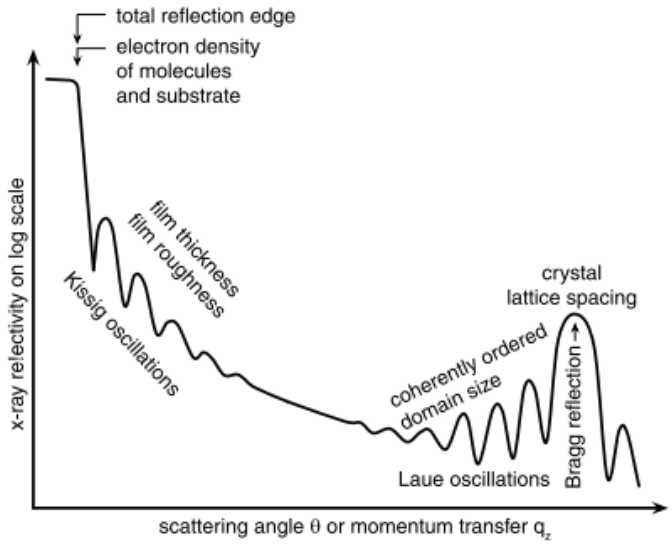

Figure 2.9: Example of X-ray reflectivity scan showing the main features and their structural origin.

be directly quantified using $D = 2\pi/\Delta\mathbf{q}_\perp$. The Kiessig fringes originate from the presence of two interfaces, independently from the crystallinity of the material in between, so they are extremely sensitive on the quality of the interfaces involved. When the Bragg's law (Eq.2.4) is satisfied, intensity maxima appear in the XRR pattern, in correspondence of the momentum $\mathbf{q_0}$ which satisfies the condition of constructive interference. From the FWHM of the Bragg peak it is possible to recover the inter-layer distance $= 2\pi/\Delta\mathbf{q_0}$, where $\mathbf{q_0}$ is the center of the peak. Additionally, side-maxima appear on the left and right sides of the Bragg-reflection. These oscillations, called Laue oscillations, stem from the thickness of the thin film. The number of oscillations corresponds to the number of coherently scattering layers as the intensity of each layer is coherently summed up resulting in $(n+1)$ layers for n oscillations. Therefore, the size of the coherently ordered domain $\Delta Domains = 2\pi/\Delta\mathbf{q}_\perp$ can be estimated from the width $\Delta\mathbf{q}_\perp$ of these oscillations. The Laue oscillations emerge from the crystalline structure of the sample, so they depend only weakly on properties like surface roughness but are sensitive to crystalline disorder.

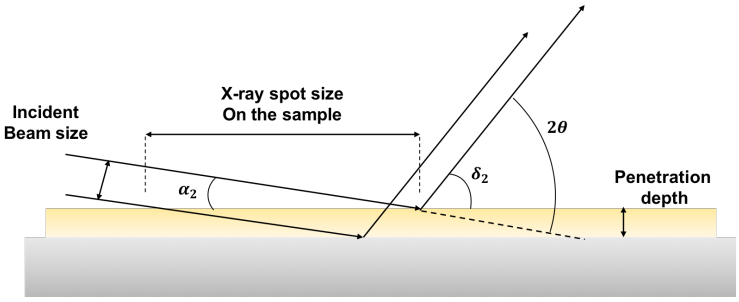

Figure 2.10: Illustration of GIXD measurement geometry. For smaller incidence angles, X-rays will be less likely to penetrate through the sample.

2.5 Grazing incidence x-ray diffraction

X-ray methods are an important tool for characterizing materials. However, for sub-micron films, the low scattering factor of carbon atoms combined with the small sample volume in thin film samples often means long time measurements. When the thin film is not chemically stable, for example when subjected to degradation by ambient atmosphere or by X-ray damage, the measurement time plays a crucial role. The first solution that can be applied to contain this drawback is to enclose the sample in an inert chamber or to modify the beam intensity. Another way to get around the problem is to modify the measurement geometry. Grazing Incidence X-Ray Diffraction (GIXD) refers to a X-ray diffraction measurement where the incidence angle is fixed to a small value, smaller than the critical angle α_c at which total internal reflection occurs. So, for an incidence angle $\alpha_i < \alpha_c$, total external reflection happens and an evanescent wave propagates under the surface. Because of the small incidence angle, the penetration depth is not so deep, as shown in Fig.2.10 resulting in a higher signal and a reduced background, making this configuration very suitable for organic thin-film samples [10] and very surface sensitive.

So, differently from XRR, GIXD is a useful technique to probe the in-plane sample structure, described from the $\mathbf{q}_{\parallel}$ component of the transfer vector. In the framework of this thesis organic thin films grown on amorphous substrates has been considered. Their particular structure present a typical configuration of their crystallites. crystallites are largely ordered parts of the material, which in the case of polycrystalline organic thin films present a common contact

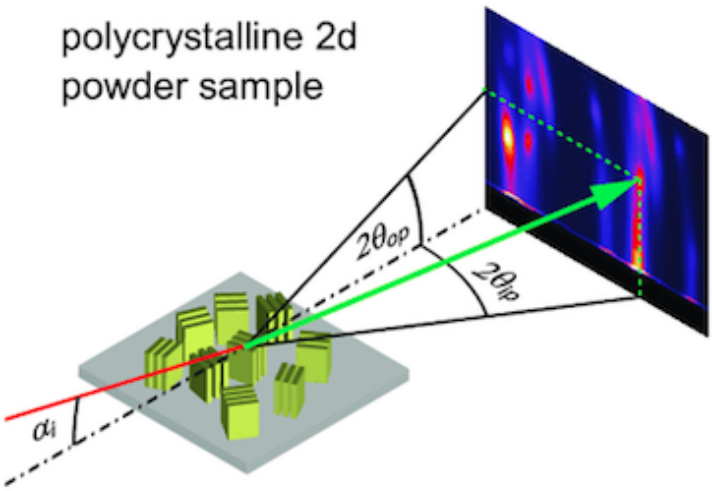

Figure 2.11: Schematic illustration of GIXD pattern arising from a 2D powder sample (top) and from aligned thin films (bottom) [52].

plane with respect to the substrate, and a random azimuthal out of plane orientation. This particular structure is called *2D powder*. In Fig.2.11 it is possible to see the GIXD pattern arising from a 2D powder sample.

Because of the Bragg's law, a given Bragg reflection is fulfilled only under a certain azimuthal sample position, and the number of reflections shown on the detector depends on how many crystallites fulfill this condition. In the case of a 2D powder sample many Bragg reflections appear on the detector thanks to the azimuthal random orientation of many crystallites. Finally, what results from the GIXD measurement is a map showing the Bragg reflections (many in the case of the 2D powder sample) in the in-plane and out-of-plane momentum space, aligned along additional structures called *truncation rods*. The truncation rods result from the crystalline surfaces, and are linear regions in the momentum space normal to the surface.

2.6 Organic molecular beam deposition

In order to grow organic molecules organic molecular beam deposition (OMBD) [53] has been performed using a portable growth camber, schematically shown in Fig.2.12, has been used.

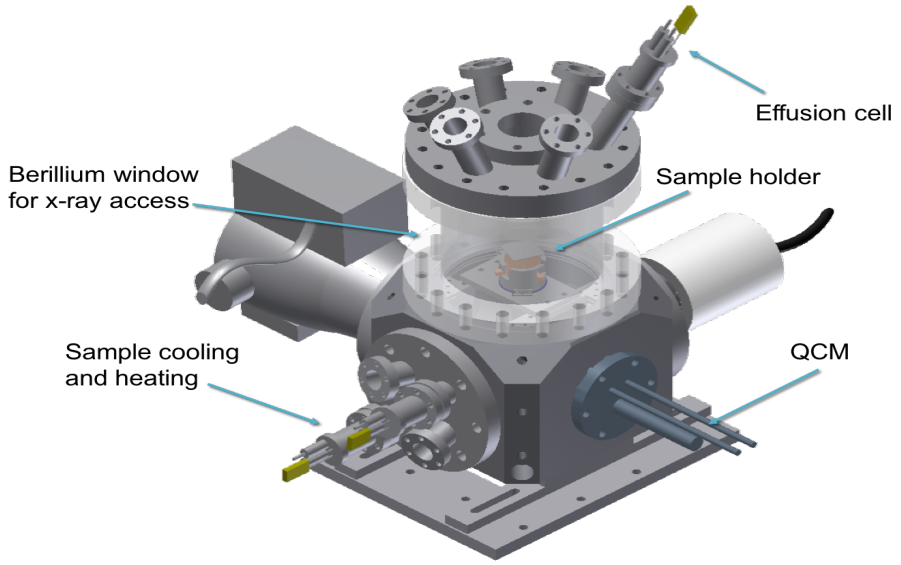

Figure 2.12: Portable vacuum growth chamber equipped with a Beryllium window, sample holder, effusion cell, QCM and feed-through for sample cooling and heating.

The main components are identified by the arrows. First of all the chamber is belted by a Beryllium widow for X-ray access, in fact Beryllium is transparent for X-rays. Then the sample holder at the center of the chamber, connected to the cooling and heating feed-through system. Additionally, the chamber is equipped with home-built effusion cells, on the top, for the thermal deposition of organic molecules. The effusion cell contains the molecular powder kept in place by some glass wool. In order to start the deposition the effusion cell is heated in order to reach the sublimation temperature of the molecules that it contains. For monitoring the film thickness during the growth, a quartz crystal micro-balance (QCM) is installed next to the sample. The pumping system of the chamber consists of a roughening and turbo pump. The growth of the organic thin films was performed at a base pressure of 10^{-8} mbar.

Chapter 3

Study of PTCDI-C_8 in UHV

The following chapter is focused on the study of the crystal structure of the archetype of organic n-type semiconductor PTCDI-C_8 (Section 1.2) in different temperature conditions. First, the procedures used to prepare the sample will be introduced. Then GIXD (Section 2.5) results will reveal the temperature-dependent crystal structure evolution of PTCDI-C_8 in a range from -60℃ to 200℃ and in UHV (10^{-7} mbar). Subsequently, the analysis methods used to retrieve the unit cell parameters from the positions of the Bragg reflections are illustrated. Finally, the results are presented. Temperature has been shown to have a strong and reversible impact on the unit cell parameters. Moreover, at high temperature 200℃ a new crystal phase appears, showing new, different values for the unit cell parameters.

3.1 Organic semiconductor PTCDI-C_8 on native Silicon Oxide

To prepare the samples, a substrate of Silicon (100) with a native oxide layer was used. The substrates were cleaned with a sequence of sonications in an ultrasonic bath with acetone, distilled water and isopropanol respectively, for a time of 15 minutes each. Afterwards a nitrogen flow was used to gently dry the substrates and remove the remaining residua. Then the growing procedure of the organic molecules were performed using OMBD as shown in Section2.6. The sublimation temperature of PTCDI-C_8 was seen at 298℃, corresponding to a deposition rate of about 4 Å/min. As a final result, a 30 nm PTCDI-C_8 thin film were grown on SiO_2

substrate.

3.2 Temperature dependent crystal structure of PTCDI-C_8 thin films

The experiment has been performed at ID03 - Surface Diffraction Beamline / ESRF [48] (Section2.1.1) where it has been possible to perform GIXD on samples of thin film made of 30 nm thick PTCDI-C_8 on SiO_2. Note that for the following described experiments an Eurotherm sensor was used to measure the temperature. The temperature calibration measurements, performed using a Pt100 reference, reported an offset about $\sim$ 2℃ between the measured and the real temperature. The sample has been put in a UHV chamber fixed on the center of the diffractometer, aligned with the X-ray beam, and the temperature of the sample has been varied between $T = -60$℃ and $T = 200$℃ while performing GIXD. The lower temperatures have been reached cooling the sample with liquid nitrogen, while the higher temperatures by heating it with a eating coil. The raw data detector images obtained from the experiment have then been treated, leading to images showing the reciprocal space where the x-axis is function of the in-plane momentum $\boldsymbol{q}_{\parallel}$ and the y-axis is function of the out-of-plane momentum $\boldsymbol{q}_{\perp}$. In Fig.3.3 the GIXD map for $T = 190$℃ is shown. Eleven diffraction rods are clearly visible, showing up to 53 Bragg reflections. These features disclose an extraordinary crystalline ordered thin film reflecting the layered and textured vertical film structure that the PTCDI-C_8 thin film assumes on the SiO_2 amorphous substrate. In fact, it is found in organic thin films grown on amorphous substrates that the random in-plane orientation of the molecular unit cell allows to detect all the Bragg reflections, regardless of the azimuthal orientation which, however, is highly ordered. Every time the Bragg condition is fulfilled, the Bragg reflections appear on the detector. For further information see Section 2.3. This peculiar geometry is pointed out in Fig.3.1 where the different in-plane and out-of-plane structures are displayed in a simplified manner.

Characteristics about the PTCDI-C_8 thin-film morphology can be deduced from XRR measurements. For example, in Fig.3.2 it is shown an XRR measurement taken at $T = 80$℃. At lower angles a considerable number of Kiessig fringes is evident, reflecting the

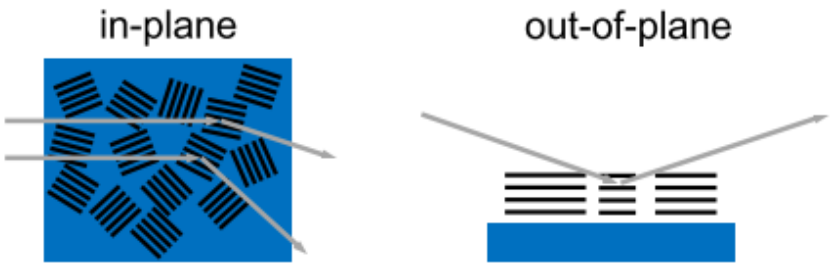

Figure 3.1: Illustration of 2D powder growth of PTCDI-C_8 on SiO_2. A random distribution of in-plane orientations, but a layered out-of-plane film structure have been observed.

presence of many high-quality interfaces, corresponding to a high quality smooth film. Moreover, from the Bragg peak and the Laue oscillations at its sides it is possible to get the crystal lattice spacing l and the coherently ordered domain size D respectively. For the case here presented it has been computed $l \simeq 17.30$ Å. In a simplified way, considering negligible contribution from the strain, the mean size of the out of plane component of the crystalline domains has been estimated from the width of the Laue oscillations, obtaining $D = 35.59$ nm. Comparing this value to the total film thickness d arising from the Kiessig fringes, $d = 37.43$ nm, it is evident that the height of the crystal grains is approximately equal to the total film thickness. This shows that the thin film has grown in an ordered and crystalline way with each crystal grain distributed along the whole film thickness. For further information about morphological studies of thermally evaporated PTCDI-C_8 see [54]. The number of Laue oscillations corresponds to the number of coherently scattering domains as the intensity of each one is summed up, resulting in $(n + 1)$-layers. In this case it is possible to identify $n = 6$ Laue oscillations, corresponding to 7 coherently scattering layers.For more information about XRR see Section 2.4.

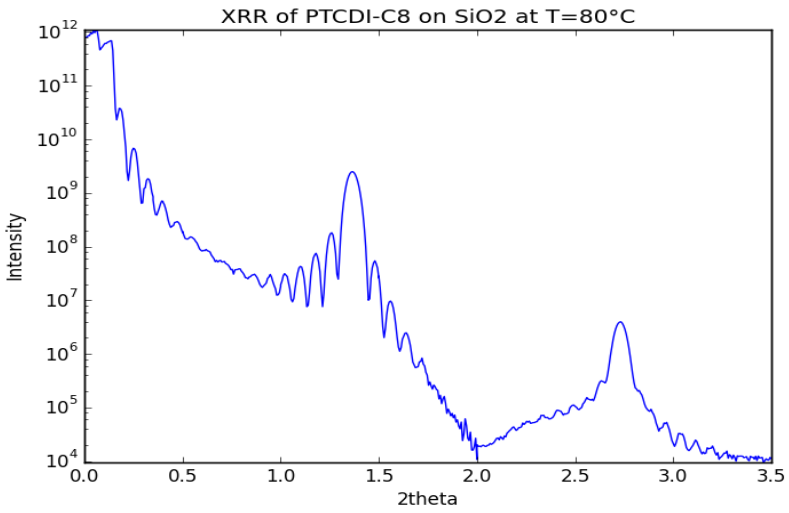

Figure 3.2: XRR curve for PTCDI-C_8 on SiO_2 at $T = 80$℃. The energy of the X-rays is $E = 13keV$, corresponding to a wavelength of $\lambda = 0.0954$ nm.

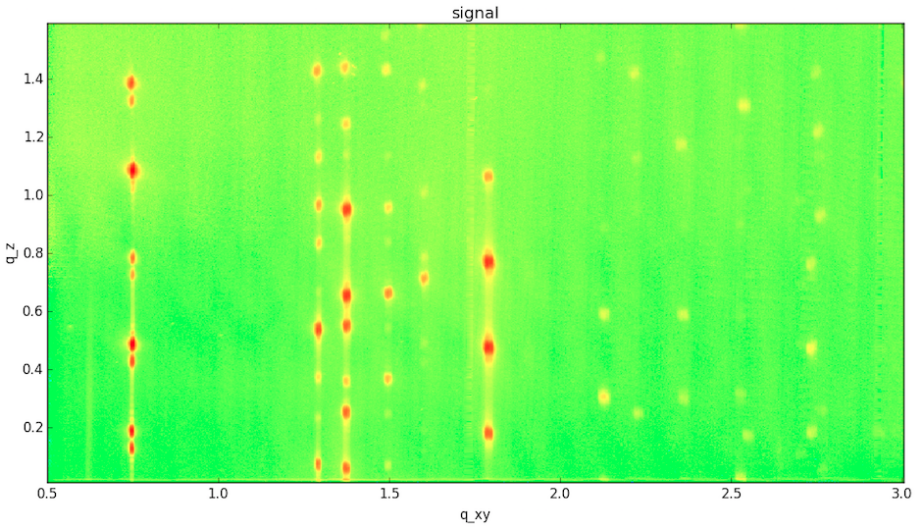

Figure 3.3: GIXD map of PTCDI-C_8 on SiO_2 at $T = 190$℃. The x-axis is given by the in-plane momentum $\boldsymbol{q}_{\parallel}$ and the y-axis by the out-of-plane momentum $\boldsymbol{q}_{\perp}$ both expressed in Angstrom [Å].

3.3 Expansion and contraction of PTCDI-C_8 unit cell parameters

The variation of the unit cell parameters with temperature has always been a subject of study in order to better understand the properties and the characteristics of a given molecule [55, 56]. To determine the crystal structure of PTCDI-C_8 film on SiO_2 Grazing Incidence X-ray Diffraction (Section2.5) was performed at the ID-03 beamline at the ESRF (Chapter 1 [44]). Moreover, to reveal the impact of temperature on the unit cell parameters the thin film temperature has been varied between $T = 60$℃ and $T = 200$℃ during the experiments. Interesting characteristics of the unit cell parameters have been pointed out. In Fig.3.4, 4 maps of the diffraction measurements are presented, showing the various diffraction rods and diffraction and diffraction spots for $T = -35$℃, $T = 0$℃, $T = 150$℃ and $T = 190$℃. From those images, it is possible to see that the Bragg reflection positions are changing while changing the temperature.

In order to have a more clear vision of these phenomenon it is useful to focus on the first five Bragg reflections $(\bar{1}01)$, (100), $(\bar{1}02)$, (101), $(\bar{1}03)$ of the first rod at $\boldsymbol{q}_{\parallel} \simeq 0.747$ [1/Å]). In Fig.3.5 it is possible to see the zoom of those reflections related to the above GIXD maps (Fig.3.4).

It is evident that the Bragg reflections are following a trend while increasing the temperature. The $(\bar{1}01)$, $(\bar{1}02)$, $(\bar{1}03)$ spots are moving upwards in the reciprocal space increasing their $\boldsymbol{q}_{\perp}$ value, while the (100), (101) are moving downwards decreasing their out-of-plane momentum value. Then, from the Bragg reflections it has been possible to extract the values of the unit cell parameters, relating the changes of the reflection positions in the reciprocal space to changes in the unit cell parameters $a, b, c, \alpha, \beta, \gamma$. This procedure will be described in the following section.

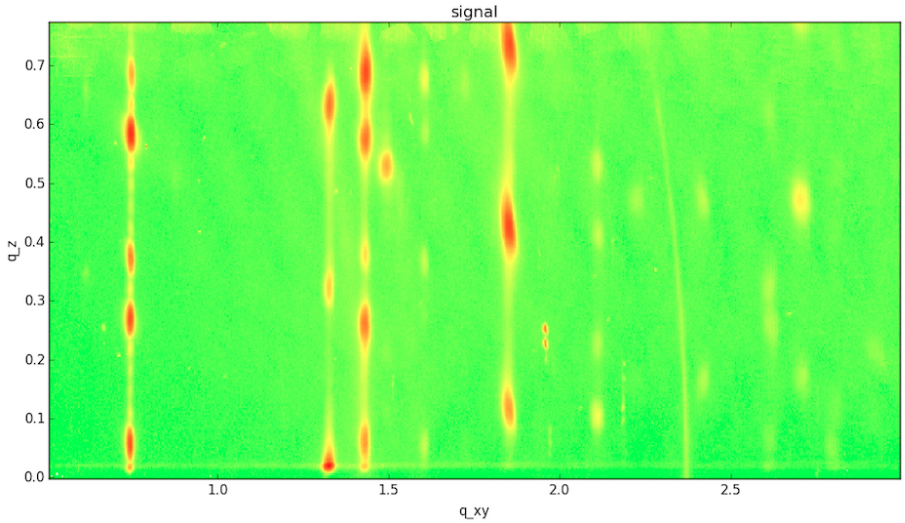
signal
0.7
0.6
0.5
0.4
0.3
0.2
0.1
0.0
q_z
1.0
1.5
2.0
2.5
q_xy

(a) $T = -35$℃

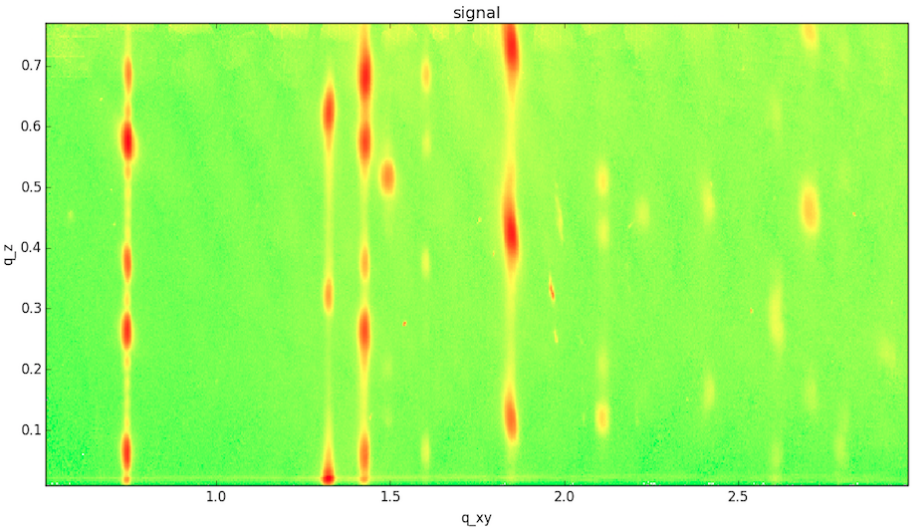
signal
0.7
0.6
0.5
0.4
0.3
0.2
0.1
q_z
1.0
1.5
2.0
2.5
q_xy

(b) $T = 0$℃

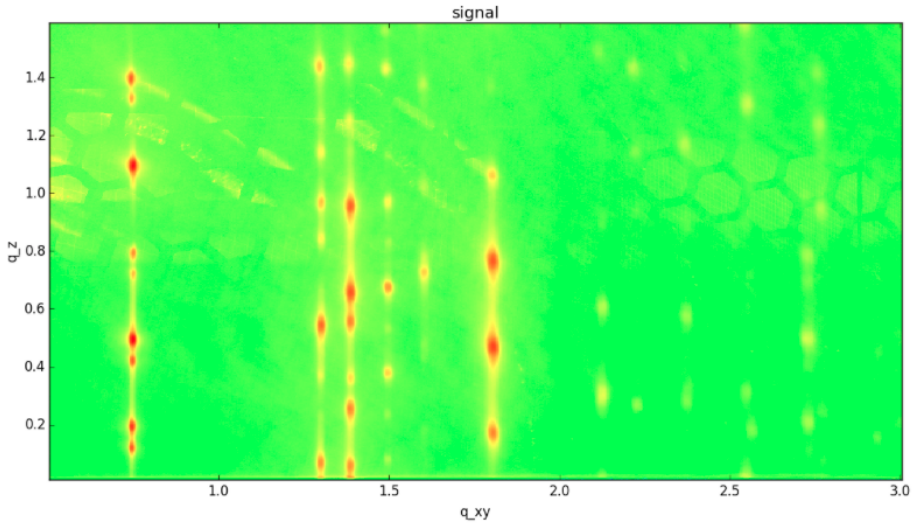

(c) $T = 150$℃

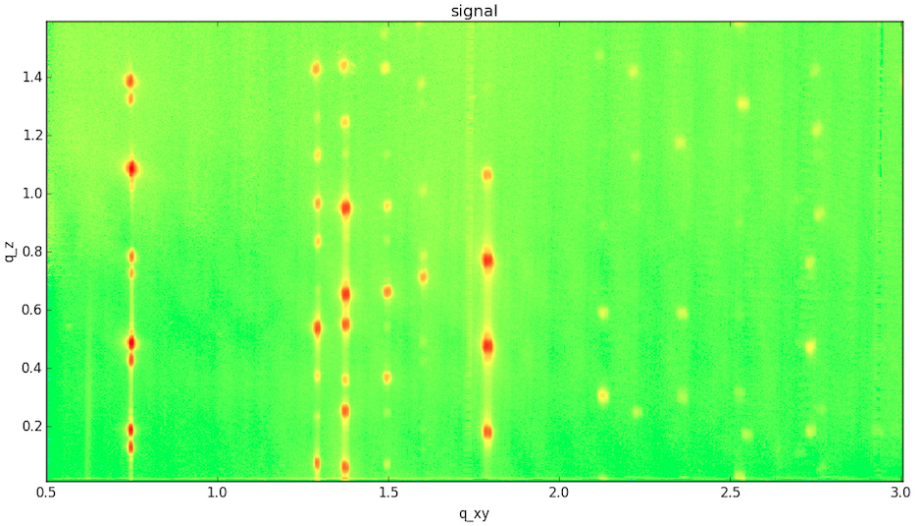

(d) $T = 190$℃

Figure 3.4: GIXD maps of PTCDI-C_8 in SiO_2 for $T = -35$℃, $T = 0$℃, $T = 150$℃, $T = 190$℃. Looking at the maps in sequence it is possible to see that the reflection spots are moving. On the first rod on the left the 1^st and the 2^nd reflections from the bootm are approaching one with the other, like the 3^{rd} and the 4^{th} and so on. On the second, third and forth rod from the left the number of reflection spots is increasing with the temperature.

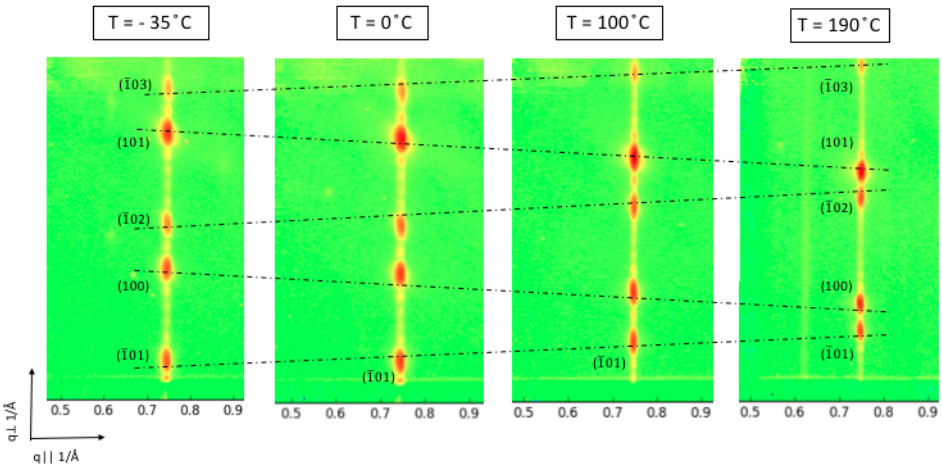

Figure 3.5: Focus on the first rod of the GIXD maps at $T = -35$℃, $T = 0$℃, $T = 150$℃, $T = 190$℃. The dashed lines show the trend followed by the $(\bar{1}01)$, (100), $(\bar{1}02)$, (101), $(\bar{1}03)$ Bragg reflections with different temperature.

3.4 Crystal phase transition of PTCDI-C_8 for $T \geq 200$℃

From the GIXD maps, another important result has been pointed out. Analyzing the images, a new different arrangement of the Bragg reflections emerges from the measurement taken at $T \geq 200$℃. Comparing the GIXD maps present in Fig.3.4 to the one recorded at $T = 200$℃ displayed in Fig.3.6 it is possible to identify at first glance a totally different scenario.

In fact, the diffraction pattern does not match any more with the one previously seen. To spot out the differences it is useful to focus on the two GIXD different maps, taken at close temperature values. Zooming again on the first five Bragg reflections $(\bar{1}01)$, (100), $(\bar{1}02)$, (101), $(\bar{1}03)$ of the first rod, Fig.3.7, we see that the Bragg reflections are placed in different $(\boldsymbol{q}_{\parallel}, \boldsymbol{q}_{\perp})$ coordinates. Moving from $T = 190$℃ (left) to $T = 200$℃ (right), number of reflections on the first rod has also increased, showing up to (102) reflection for the same $\mathbf{q}_{\perp}$ range. Moreover, for the first rod the $\boldsymbol{q}_{\parallel}$ position has changed from $\boldsymbol{q}_{\parallel} \simeq 0.747$ [1/Å] for $T = 190$℃ to $\boldsymbol{q}_{\parallel} \simeq 0.625$ [1/Å] at $T = 200$℃.

This unexpected diffraction pattern found for $T \geq 200$℃ corresponds to a different crystal phase of the PTCDI-C_8 molecule. Computing the values for the unit cell parameters, it has been demon-

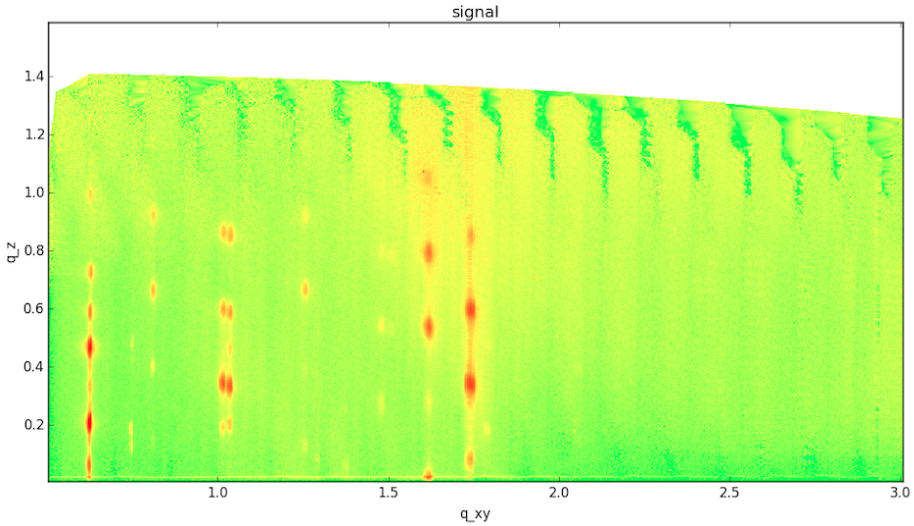

Figure 3.6: GIXD map taken with $T = 200$℃. A new crystal phase is visible.

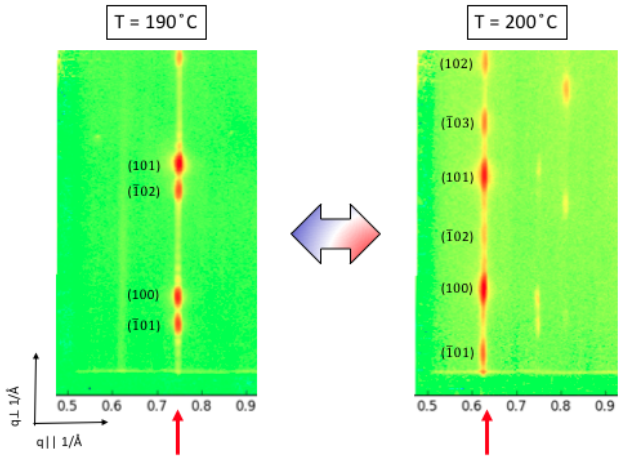

Figure 3.7: Detail of the first rod for the two GIXD maps taken at $T = 190$℃ (left) and $T = 200$℃ (right).

strated that the new crystal phase corresponds to a modified unit cell.

3.5 Data analysis software

For the data analysis a statistical data processing formalism developed by Linus Pithan has been used [23]. In Fig. 3.8 a diagram showing the main passages of the data processing is present. First, the diffraction patterns are calculated and compared to the ones generated by manually masking the GIXD image. Then, exploiting the latin hypercube sampling method within Monte Carlo simulations, sets of unit cell parameters $(a, b, c, \alpha, \beta, \gamma)$ are systematically generated. Consequently, the number of calculated reflections falling inside the masked area is counted to define a measure describing the agreement between the calculated reflections and the experimental data. If this count exceeds a certain threshold, the set of unit cell parameters will be saved as suitable candidate for further processing. Finally, a statistical evaluation through a Gaussian fit of the hits as a function of the unit cell parameters gives the unit cell parameters describing the experimental data best.

Additionally, for the above mentioned data processing, it is important to set a reasonable range for each unit cell parameter. In fact, the possible combinations of suitable unit cells are computed combining the parameters within those ranges. For deducing reasonable ranges of values for $a, b, c, \alpha, \beta, \gamma$ of the unknown high temperature crystal phase a new Python code has been developed in the framework of this thesis. Consequently, it has been possible to index the Bragg reflections with Miller indices and find suitable initial parameter ranges for the statistical analysis. Using this new tool, the indexing is straightforward: it is possible to manually and independently change the values of then unit cell parameters thanks to a set of sliders, in order to move the Bragg reflections' and rods' markers and make them match with the reflections of the GIXD image lying underneath.

In Fig.3.9 an image of the above mentioned program is present. On the left there are the $a, b, c, \alpha, \beta, \gamma$ sliders that can be manually and independently moved. For every change in the sliders the Bragg reflections' and rods' markers move coherently in the reciprocal space. The GIXD map is uploaded and lies underneath the markers so it is possible to move the sliders in order to match the

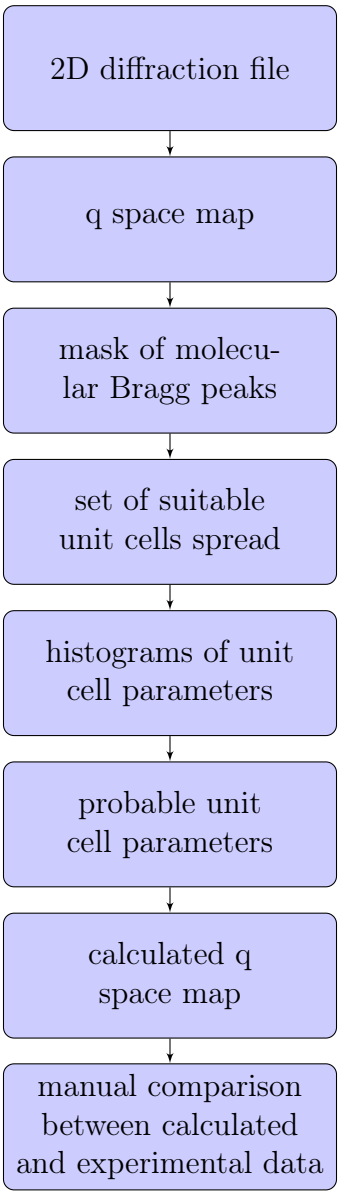

Figure 3.8: Flow diagram of the step-by-step of the data processing of the 2D GIXD images

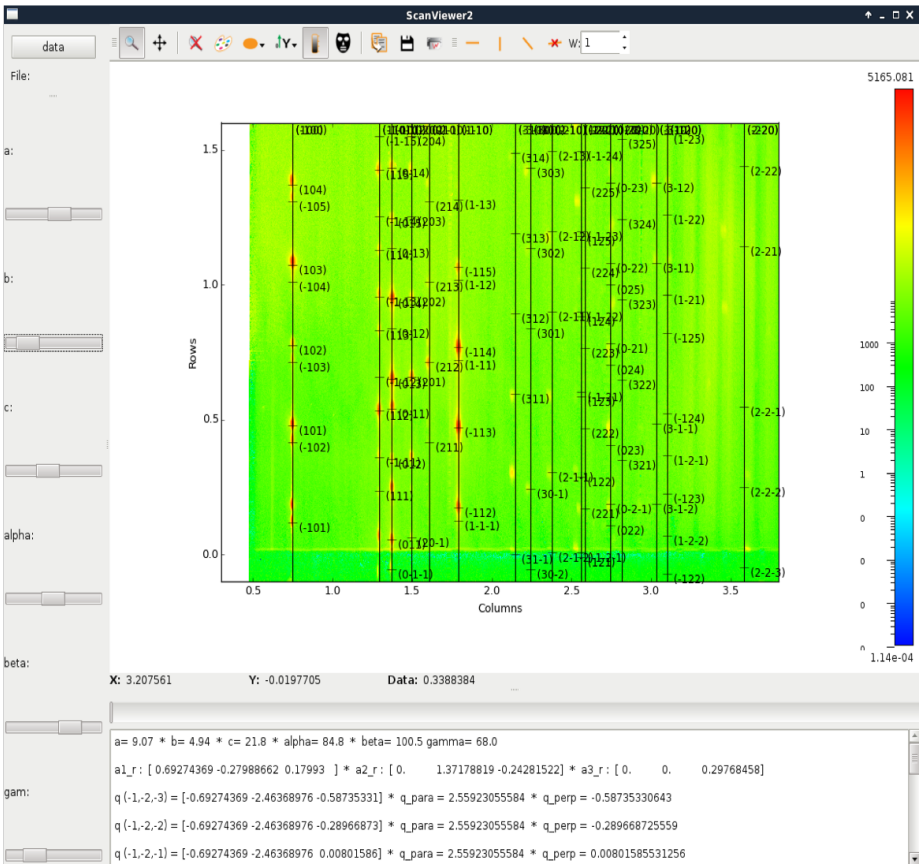

Figure 3.9: Outlook of the indexing program: the reflections' markers are manually moved in order to match the reflections of the GIXD image.

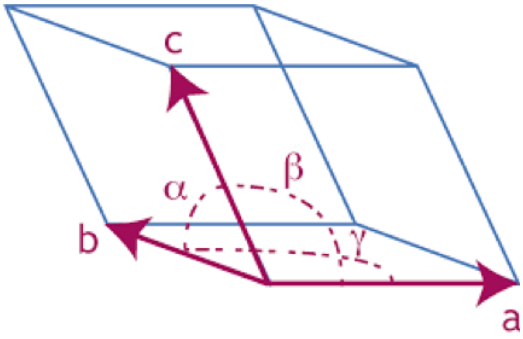

Figure 3.10: Reference system for the unit cell parameters in the real space.

reflections of the current image. The unit cell parameters and the indexing are shown during the whole process.
In the following lines the physical relations used to build up the code will be presented. The real space reference unit cell used for the PTCDI-C_8 film is shown in Fig.3.10, where the *ab*-plane identifies the in-plane geometry, while the *c* parameter belongs to the out-of-plane geometry both in the real space.

In order to retrieve the real space unit cell parameters we need to relate the real space to the reciprocal one, which is mapped from the GIXD measurements. The real space lattice can be described by the position vectors $\mathbf{R}$ of the form:

$$\boldsymbol{R} = n_1\boldsymbol{a}_1 + n_2\boldsymbol{a}_2 + n_3\boldsymbol{a}_3 \tag{3.1}$$

where the $\mathbf{a_i}$ are the basis vectors which span the whole lattice and the n_i are integer numbers. The set of all wave vectors $\mathbf{Q}$ that produce waves with the same periodicity of the real lattice is known as its reciprocal lattice. In this case it is possible to refer at the real space also as the direct space. Analytically, $\mathbf{Q}$ belongs to the reciprocal lattice of the direct lattice made up of points $\mathbf{R}$ provided that $e^{i\mathbf{Q}\cdot(\mathbf{r}+\mathbf{R})} = e^{i\mathbf{QR}}$ holds for any $\mathbf{r}$ and $\mathbf{R}$, and that $e^{i\mathbf{QR}} = 1$. Then, the reciprocal space can be generated by the three primitive vectors $\mathbf{b_{1,2,3}}$:

$$\mathbf{b_1} = 2\pi\frac{\mathbf{a_2}\times\mathbf{a_3}}{\mathbf{a_1}\cdot(\mathbf{a_2}\times\mathbf{a_3})} \tag{3.2}$$

$$\mathbf{b_2} = 2\pi\frac{\mathbf{a_3}\times\mathbf{a_1}}{\mathbf{a_1}\cdot(\mathbf{a_2}\times\mathbf{a_3})} \tag{3.3}$$

$$\mathbf{b_3} = 2\pi \frac{\mathbf{a_1} \times \mathbf{a_2}}{\mathbf{a_1} \cdot (\mathbf{a_2} \times \mathbf{a_3})} \tag{3.4}$$

Notice that the denominator of the above equations corresponds to the volume of the direct space unit cell. So, any vector $\mathbf{Q}$ can be written as a combination of the $\mathbf{b_i}$:

$$\mathbf{Q} = k_1\mathbf{b_1} + k_2\mathbf{b_2} + k_3\mathbf{b_3} \tag{3.5}$$

where the k_i are integers. Every Bragg reflection spot can be identified in the reciprocal space by a vector $\mathbf{Q}$ where the (k_1,k_2,k_3) are none other than the (h,k,l) Miller indices, which identify the crystallographic direction of the Bragg plane involved in the reflection considered. So for every Bragg reflection we can write its $\mathbf{Q}$ vector:

$$\mathbf{Q} = h\mathbf{b_1} + k\mathbf{b_2} + l\mathbf{b_3} \tag{3.6}$$

which in the GIXD maps appears in its $\mathbf{q}_{\parallel}$ and $\mathbf{q}_{\perp}$ components:

$$\mathbf{Q} = \mathbf{q}_{\parallel} + \mathbf{q}_{\perp} \tag{3.7}$$

$$\boldsymbol{q}_{\parallel} = \sqrt{(h\boldsymbol{b_1})^2 + (k\boldsymbol{b_2})^2} \tag{3.8}$$

$$\boldsymbol{q}_{\perp} = l\boldsymbol{b_3} \tag{3.9}$$

Those components maps respectively the in-plane geometry and the out-of-plane geometry of the lattice in the reciprocal space. Now, explicating the $\mathbf{a_{1,2,3}}$ in relation to the real space unit cell parameters, the connection between the reciprocal space reflections and the $a, b, c, \alpha, \beta, \gamma$ parameters is straightforward [57].

$$\boldsymbol{a_1} = \begin{bmatrix} a \\ 0 \\ 0 \end{bmatrix} \tag{3.10}$$

$$\boldsymbol{a_2} = \begin{bmatrix} b\cos\gamma \\ b\sin\gamma \\ 0 \end{bmatrix} \tag{3.11}$$

$$\boldsymbol{a_3} = \begin{bmatrix} c\cos\beta \\ c\cos\alpha - \frac{\cos\gamma\cos\beta}{\sin\gamma} \\ \sqrt{c^2 - (c\cos\beta)^2 - (c\cos\alpha - \frac{\cos\gamma\cos\beta}{\sin\gamma})^2} \end{bmatrix} \tag{3.12}$$

Finally, thanks to the mentioned relations, it has been possible to associate at every ($\boldsymbol{q}_{\parallel}$, $\boldsymbol{q}_{\perp}$) which define a Bragg reflection, the corresponding Miller indices (h, k, l) which allow to construct the vector $\mathbf{Q}$ that is connected to the direct space vectors $\mathbf{a_1}, \mathbf{a_2}, \mathbf{a_3}$ and so, with the unit cell parameters $a, b, c, \alpha, \beta, \gamma$.

3.6 Dependence of unit cell parameters with temperature

The first result which appears from the experiment is the dependence of the unit cell parameters on temperature. In the temperature range ($T = -60$℃ - $T = 200$℃) spanned during the measurements a change in the Bragg reflections positions is clearly visible, as it is shown in the detail of the first rod present in Fig.3.5 and as it has been previously discussed. This change in the position of the Bragg reflections is caused by a modification in the crystal structure, in particular a change of the thin film unit cell parameters. So, from the data analysis performed the values of $a, b, c, \alpha, \beta, \gamma$ have been extracted for each temperature. The unit cell volume has consequently been calculated in according to Eq.3.13:

$$V_{\mathrm{uc}} = abc\sqrt{1 + 2\cos\alpha\cos\beta\cos\gamma - \cos^2\alpha - \cos^2\beta - \cos^2\gamma} \tag{3.13}$$

In the following Table3.1 the values of the unit parameters are shown for different temperatures.

Then, for *a, b, c* parameters the thermal expansion coefficient has been computed. The thermal expansion coefficient is expressed by:

$$\alpha = \frac{\Delta l}{\Delta T}\frac{1}{l_1} \tag{3.14}$$

where $\Delta l = l_2 - l_1$ corresponds to the change in length, $\Delta T = T_2 - T_1$ to the change in temperature and l_1 is the initial length.

Table 3.1: Unit cell parameters for different temperatures.

.	$T = -35$℃	$T = 40$℃	$T = 112$℃	$T = 190$℃
a	9.19 ± 0.01 Å	9.19 ± 0.02 Å	9.12 ± 0.02 Å	9.09 ± 0.03 Å
b	4.79 ± 0.01 Å	4.32 ± 0.01 Å	4.89 ± 0.01 Å	4.95 ± 0.01 Å
c	21.22 ± 0.09 Å	21.49 ± 0.11 Å	21.66 ± 0.07 Å	21.74 ± 0.07 Å
α	87.54 ± 0.20 °	86.95 ± 0.25 °	85.29 ± 0.29 °	84.76 ± 0.24 °
β	106.60 ± 0.24 °	105.32 ± 0.27 °	102.11 ± 0.23 °	100.50 ± 0.24 °
γ	66.61 ± 0.35 °	66.87 ± 0.19 °	67.40 ± 0.22 °	67.79 ± 0.22 °

Table 3.2: Unit cell volume for different temperatures.

.	$T = -35$℃	$T = 40$℃	$T = 112$℃	$T = 190$℃
$V_{unitcell}$	808.53 Å^3	832.68 Å^3	857.66 Å^3	876.56 Å^3

For the *a, b, c* the following values have been respectively obtained for $T_1 = -35$℃ and $T_2 = 190$℃: $\alpha_a = -4.84 \cdot 10^{-5} \mp 0.40\ 1/K$, $\alpha_b = 4.75 \cdot 10^{-5} \pm 0.13\ 1/K$, $\alpha_c = 3.48 \cdot 10^{-5} \pm 0.001\ 1/K$. Materials usually expand upon heating as the inter-atomic bond length increases due to "longitudinal vibrations". So, an increase of temperature causes an increase of the anharmonic vibrations of the involved atoms around their equilibrium positions. The molecular packing is not affected significantly by the temperature change, usually leading to a small positive thermal expansion coefficient of about $< 20 \cdot 10^{-6}\ 1/K$ [58]. In this case the *a*-axis shows a large negative thermal expansion coefficient comparing to the standard behaviour above mentioned. In contrast the *b,c*-axis counterbalance this situation, showing large positive thermal expansion coefficients. Negative thermal expansion has been observed also in metal-oxides [59] and organic-crystals [60, 61]. In all cases the negative thermal expansion is accompanied by structural changes, in particular the change of molecular orientations within the molecular solid. From those values the different unit cell volumes have been computed. The results are illustrated in Table 3.2

Moreover, from the scatter plots in FIG.3.11 the trend of each parameter, highlighted by the red linear regression line, catches the eye. While increasing the temperature b, c, γ and the unit cell volume are increasing (positive slope in the regression line), while a, α, β are decreasing (negative slope).

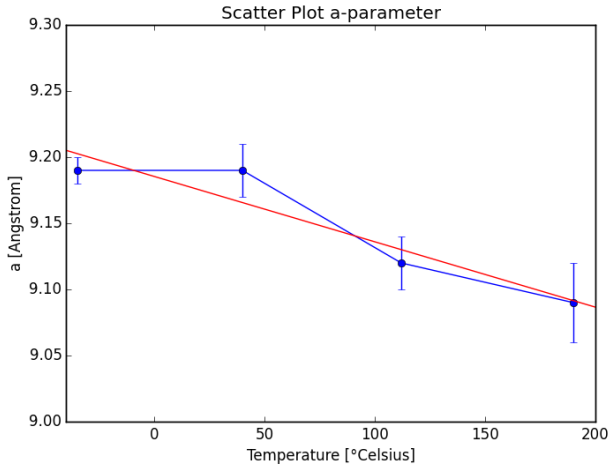

(a) Parameter a

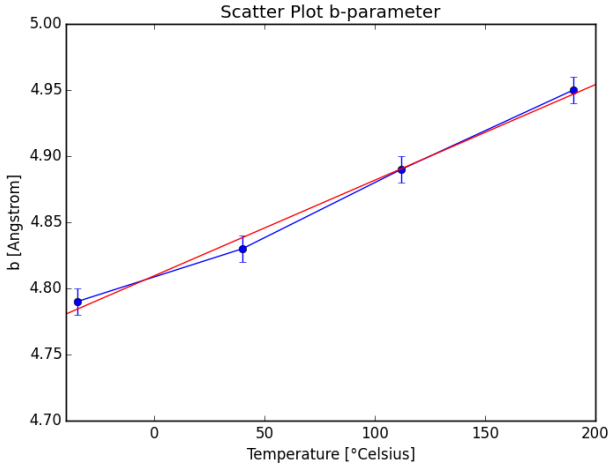

(b) Parameter b

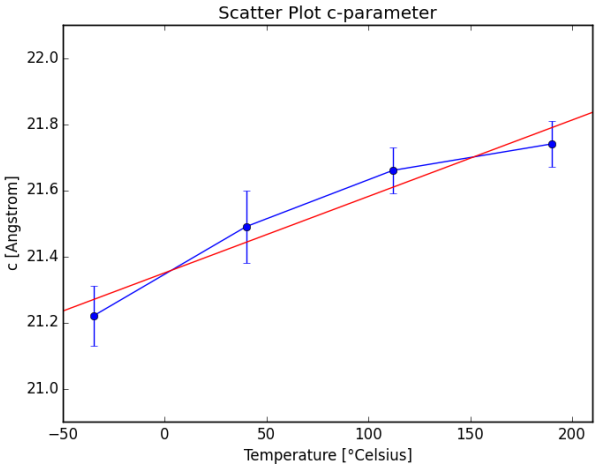

(c) Parameter c

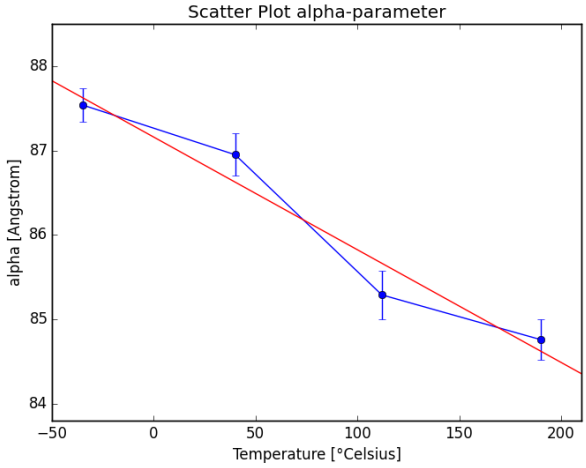

(d) Parameter α

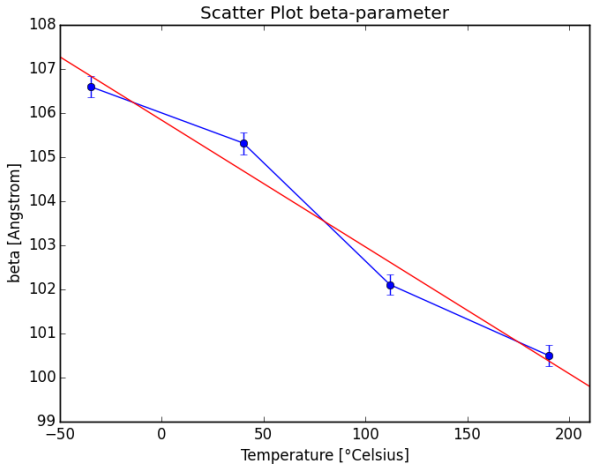

(e) Parameter β

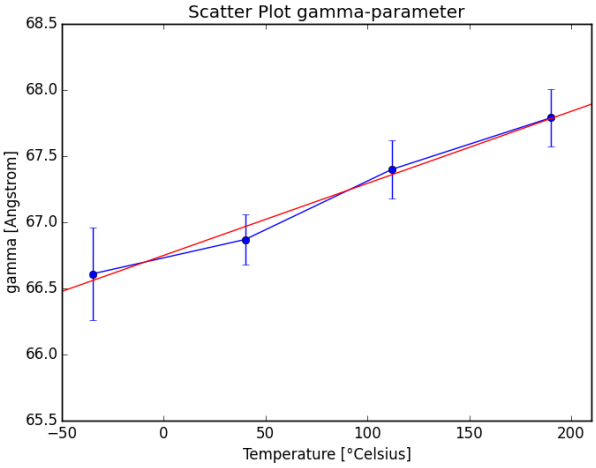

(f) Parameter γ

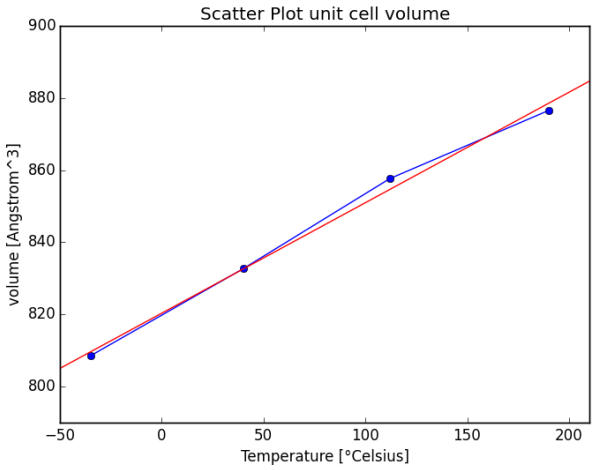

(g) Unit cell volume

Figure 3.11: Scatter plots showing the variation of the unit cell parameters and unit cell volume of PTCDI-C_8 with different temperatures.

It is worth noting that the PTCDI-C_8 thin film unit cell differs considerably from the bulk structure obtained by Briseno et al. from millimeter-long needles of PTCDI-C_8 single-crystal X-ray crystallography: ($a = 8.50$ Å, $b = 4.68$ Å, $c = 19.72$ Å, $\alpha = 85.99°$, $\beta = 91.57°$, $\gamma = 82.79°$) [35]. The differences could be attributed to the different energetics within thin film growth compared to single crystal growth as additional surface energies appear. Also the volume is clearly increasing while increasing the temperature going from a value of $V_{unitcell} = 808.53$ Å^3 at $T = -35$℃ up to a value of $V_{unitcell} = 876.56$ Å^3 at $T = 190$℃. Generally, PTCDI-C_8 crystallizes in a triclinic crystal structure ($a \neq b \neq c$, $\alpha \neq \beta \neq \gamma \neq 90°$) with one molecule per unit cell. Consequently, from the dimension of the unit cell obtained, an increased c-axis and a higher value of the γ-angle let us deduce that with increasing the temperature the PTCDI-C_8 molecule is assuming a more upright orientation with respect to the surface. This result is a natural deduction also in the light of the results obtained by Krauss et al.[25] regarding the molecular orientation of PTCDI-C_8 within the unit cell, shown in Fig.3.12.

For a further investigation of the impact of temperature on the

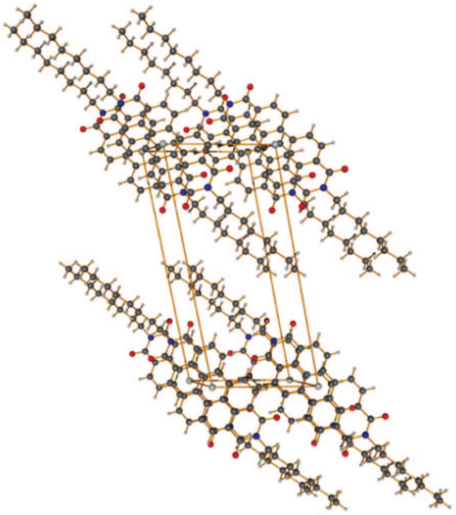

Figure 3.12: PTCDI-C_8 molecular arrangement within the unit cell obtained by Krauss et al.[25].

molecular orientations of PTCDI-C_8 see [62]. In the below Fig.3.13 a simulation of the unit cells obtained at $T = -35$℃ and $T = 190$℃ is present. The image clearly shows the increase in the unit cell volume with temperature.

The second result that has been obtained regards the transition to a new, different and reversible crystal phase happening at $T \geq 200$℃. The map in Fig.3.6 acquired at $T = 200$℃ clearly shows a reflection pattern that is substantially different from the one in Fig.3.3 acquired just 10℃ below, at $T = 190$℃. From the data analysis of the unknown high temperature crystal phase, new, different values for the unit cell parameters have been extracted. In Table 3.3 it is possible to see a direct comparison for the two nearest temperatures below and above the crystal phase transition.

All the parameters have changed, showing an increment in the unit cell volume which has almost doubled from $V_{unitcell} = 876.56$ Å^3 to $V_{unitcell} = 1855.33$ Å^3. From literature it is known that PTCDI-C_8 thin film accommodates one molecule per unit cell [25]. By increasing the temperature and doubling the unit cell volume, it is worth thinking that also the number of molecules per unit cell doubles. So, being the unit cell populated by two PTCDI-$_8$ molecules at room temperature, corresponding to volume of $V_{unitcell} = 876.56$ Å^3, at $T \simeq 200$℃ for $V_{unitcell} = 1855.33$ Å^3 four molecules are expected. In

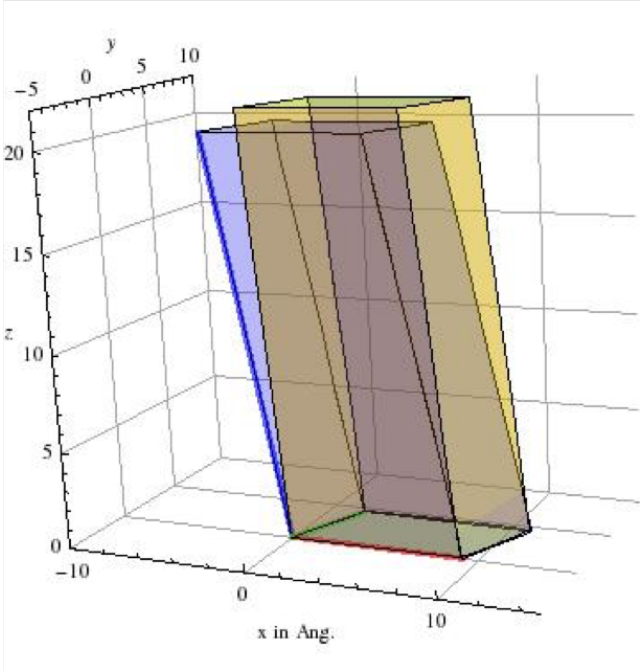

Figure 3.13: Simulation of the unit cell structure at $T = -35$℃ (blue) and $T = 190$℃ (yellow). X-axis and y-axis are expressed in Angstrom [Å].

Table 3.3: Unit cell volume for different temperatures.

.	$T = 190$℃	$T = 200$℃
a	9.09 ± 0.03	10.03 ± 0.03 Å
b	4.95 ± 0.01	7.76 ± 0.03 Å
c	21.74 ± 0.07	25.34 ± 0.14 Å
α	84.76 ± 0.24	$99.33 \pm 0.40°$
β	100.50 ± 0.24	$107.50 \pm 0.16°$
γ	67.79 ± 0.22	$88.78 \pm 0.24°$
$V_{unitcell}$	876.56 Å^3	1855.33 Å^3

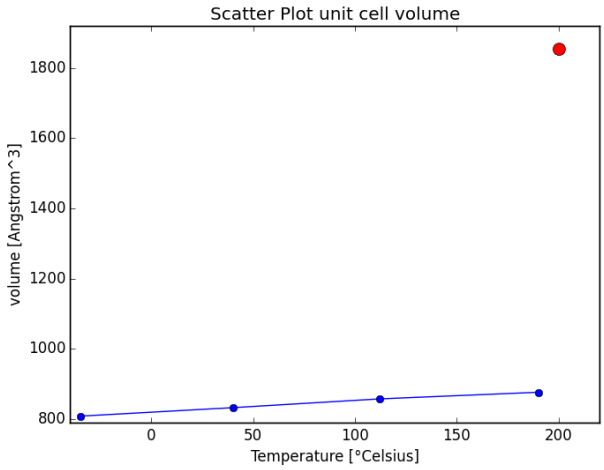

Figure 3.14: Scatter plot showing the variation of the unit cell volume of the two different crystal phases of PTCDI-C_8 (blue for ($T = -35$℃ $\div$ $T = 190$℃), red for $T = 200$℃)

Fig.3.14 a scatter plot comparing the increasing trend of the unit cell volume and the unit cell volume for the high temperature phase is shown. The red spot, corresponding to $V_{unitcell} = 1855.33$ Å^3, is completely out of trend reflecting the doubling of the unit cell volume.

It is also interesting to point out that the in-plane γ-angle has significantly increased from $\gamma = 67.79°$ to $\gamma = 88.78°$, leading to an almost monoclinic unit cell ($a \neq b \neq c, \alpha = \gamma = 90° \neq \beta$). In this case the thermal expansion coefficient has been computed for the temperature interval ($T = 190$℃ $- T = 200$℃), obtaining: $\alpha_a = 0.01 \pm 0.067$ $1/K$, $\alpha_b = 0.057 \pm 0.016$ $1/K$, $\alpha_c = 0.073 \pm 0.12$ $1/K$. These extremely high values reflect the doubling of the unit cell volume. Two simulations of the above mentioned unit cell configurations are showed in Figs.3.15a3.15b. From these simulations the change in the unit cell volume of the two different temperatures it is even more evident.

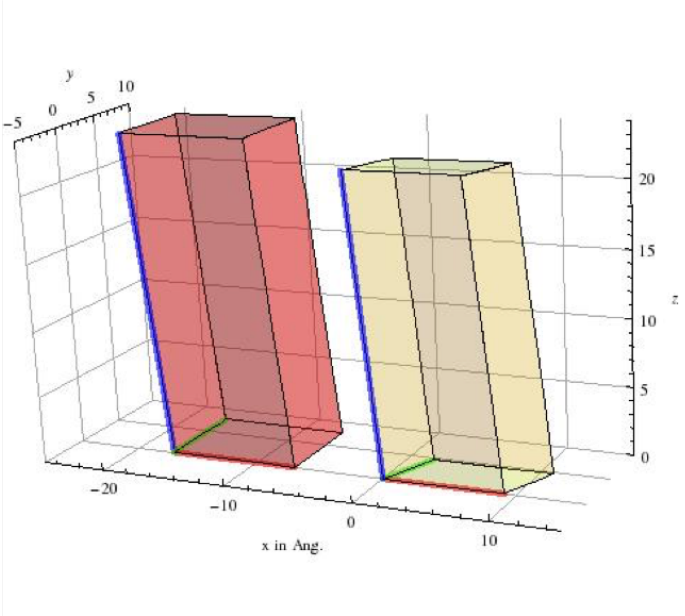

(a) Front view

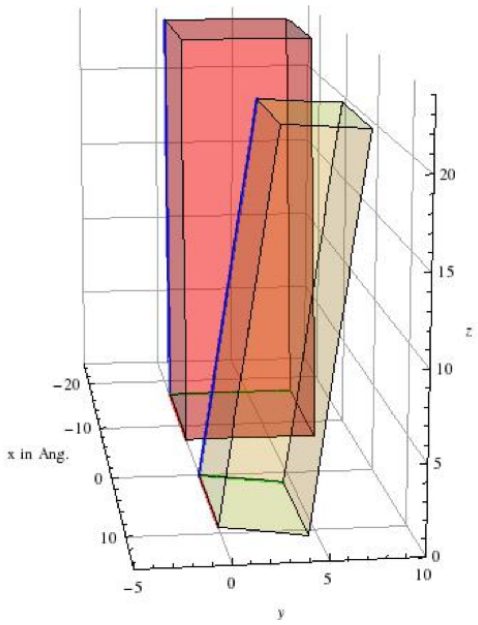

(b) Lateral view

Figure 3.15: Simulation of the unit cell structure at $T = 200$℃ (red) and $T = 190$℃ (yellow). X-y-z-axis are expressed in Angstrom [Å].

3.7 Reversibility of the two different crystal phases

In the previous section it has been shown that when increasing the temperature from $T = 190$℃ to $T = 200$℃, a new crystal phase of the PTCDI-C_8 thin film appears. From this condition, another interesting result can be retrieved. In fact, lowering again the temperature of the sample from $T = 200$℃ to lower values, the thin film crystal phase changes again to its previous configuration. This reversibility property of PTCDI-C_8 crystal phase can be seen both from XRR and GIXD measurements. In Figs.3.16, 3.17 two different XRR measurements taken at the same temperature, $T = 175$℃, are shown. The first one has been recorded during while increasing the temperature, then once $T = 200$℃ has been reached, the temperature has been decreased, recording the second XRR again at $T = 175$℃.

From the XRR plots it is possible to see that the crystallinity of the film has been preserved, in fact for the second measurement (3.17) both the Kiessig fringes and the Laue oscillations are clearly visible, showing that the film has the same thickness as before and the homogeneity and the Bragg condition have not been modified. Considering GIXD images we can compare for example the maps taken at $T = 60$℃ (Fig.3.18) while increasing the temperature up to $T = 200$℃, and at $T = 40$℃ (Fig.3.19) while decreasing it.

Going from the high temperature crystal phase at $T = 200$℃ back again to lower temperatures, the room temperature crystal phase is recovered showing the same reflections pattern that was initially present. The truncation rods are placed at the same $\mathbf{q}_{\parallel}$ values (for example the first rod is still at $\mathbf{q}_{\parallel} \simeq 0.747[1/\text{Å}]$) and the Bragg reflections of the two maps correspond one to anther. Moreover, the unit cell parameters that have been obtained for $T = 40$℃ are in perfect accord to the results illustrated in the previous paragraph 3.6: $a = 9.16$ Å, $b = 4.82$ Å, $c = 21.58$ Å, $\alpha = 86.95°, \beta = 105.32°, \gamma = 66.88°$.

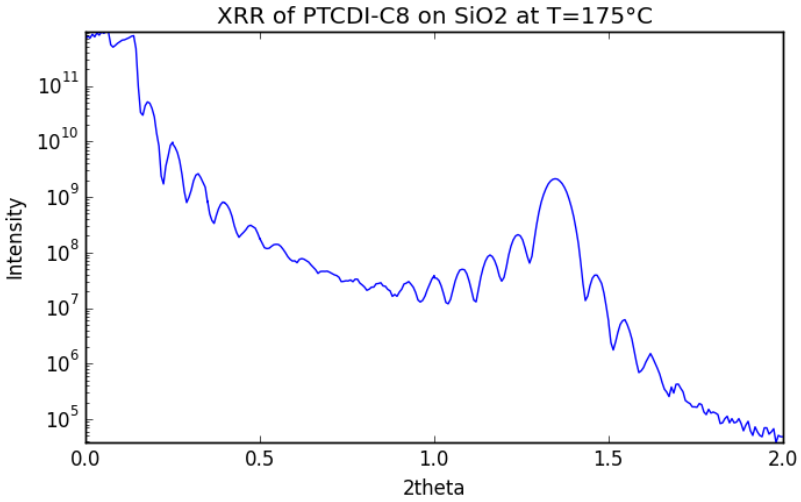

Figure 3.16: XRR measurement of PTCDI-C_8 at $T = 175$℃, in the increasing-temperature cycle. The energy of the X-rays is $E = 13$ keV, corresponding to a wavelength of $\lambda = 0.0954$ nm.

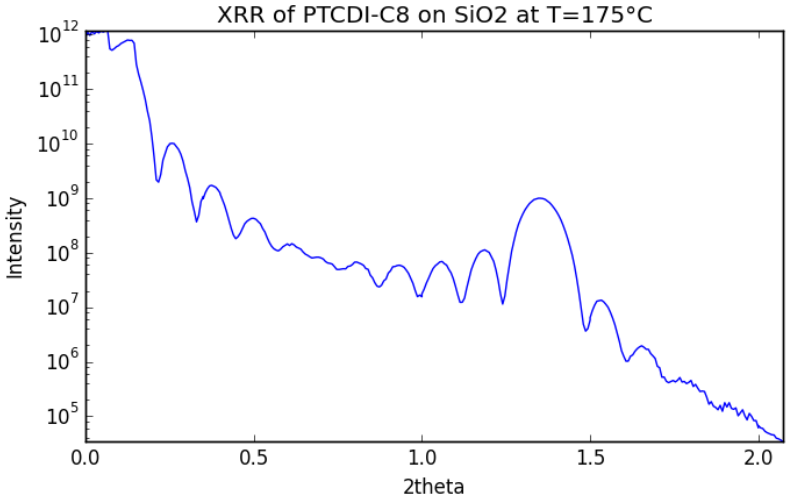

Figure 3.17: XRR measurement of PTCDI-C_8 at $T = 175$℃, in the decreasing-temperature cycle.The energy of the X-rays is $E = 13$ keV, corresponding to a wavelength of $\lambda = 0.0954$ nm.

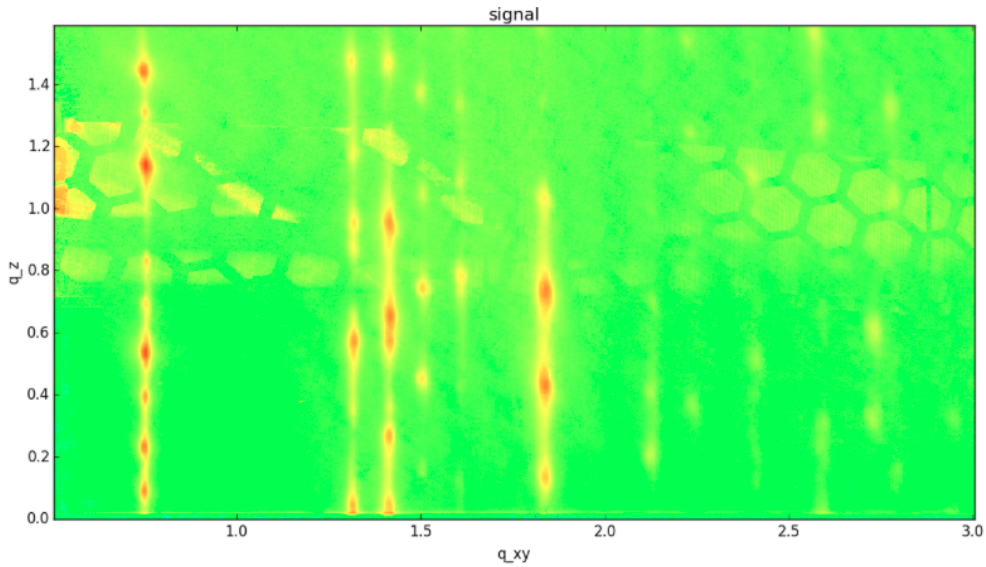

Figure 3.18: GIXD map of PTCDI-C_8 thin film taken at $T = 60$℃ while increasing the temperature.

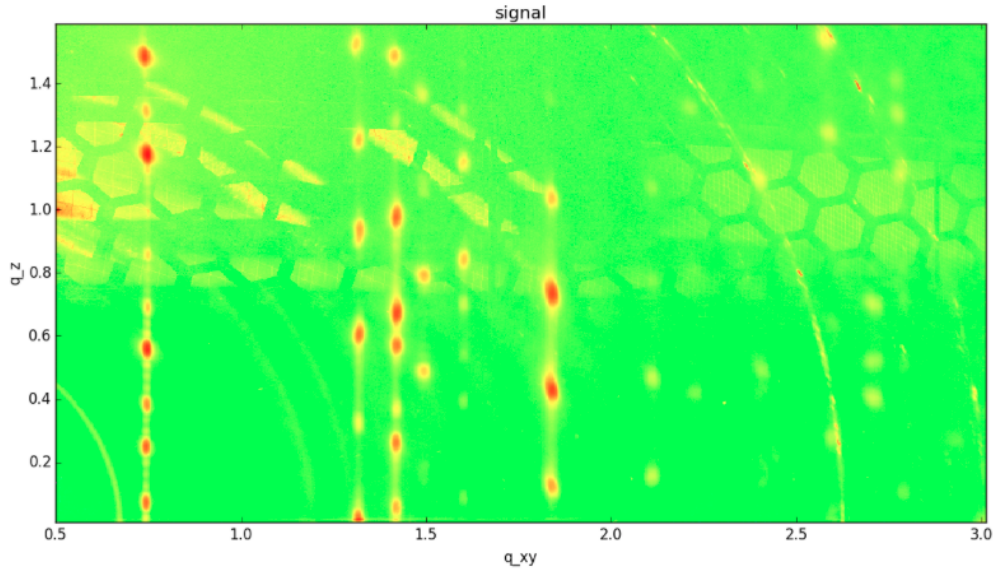

Figure 3.19: GIXD map of PTCDI-C_8 thin film taken at $T = 60$℃ while increasing the temperature.

3.8 Results

It is shown that GIXD measurements of PTCDI-C_8 thin films on SiO_2 exhibit the reversible and continuous motion of the unit cell parameters upon changing the temperature of the sample. Moreover, for $T = 200$℃ a new, different and reversible Bragg diffraction pattern shows up, leading to new and previously unknown unit cell parameters, off trend with respect to the values recorded at lower temperature, which correspond to an almost doubled unit cell volume. In Fig.3.20 the scatter plots are illustrating the overall situation: the blue spots represent the unit cell parameters and volume for the range ($T = -35$℃ - $T = 190$℃), while the red spots represent the new high temperature crystal phase of PTCDI-C_8 at $T \geq 200$℃.

For the low temperature crystal phase the trand of the unit cell parameters is clear: a, α, β are decreasing with higher temperatures while b, c, γ are increasing. Considering also the results for $T = 200$℃, the difference between the two phases is outstanding: the new crystal phase is completely off trend with respect to the one investigated for $T < 200$℃. The values of the unit cell parameters have increased, doubling the unit cell volume from $V_{unitcell} \simeq 876.56$ Å^3, at room temperature, to $V_{unitcell} = 1855.33$ Å^3 at $T \simeq 200$℃.

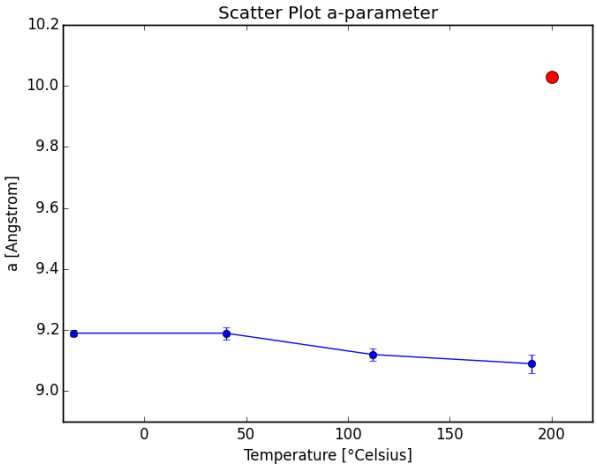

(a) Parameter a

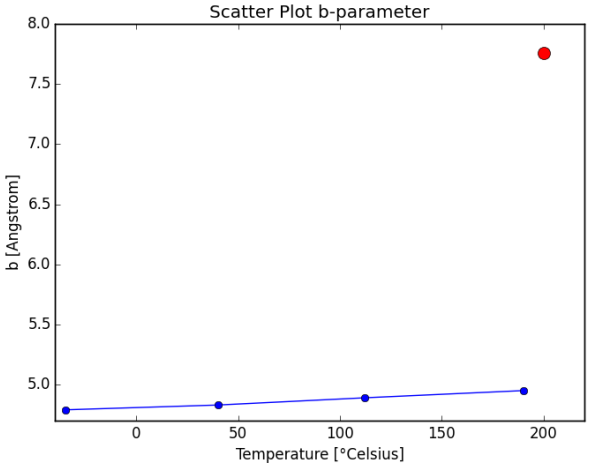

(b) Parameter b

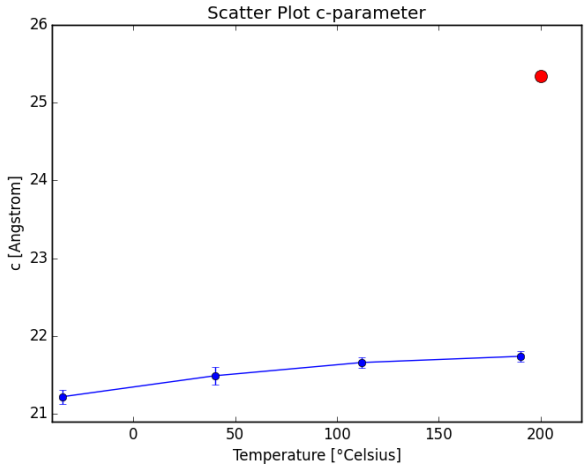

(c) Parameter c

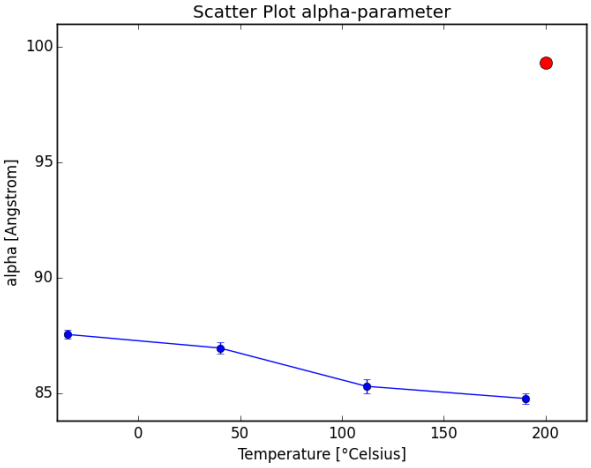

(d) Parameter α

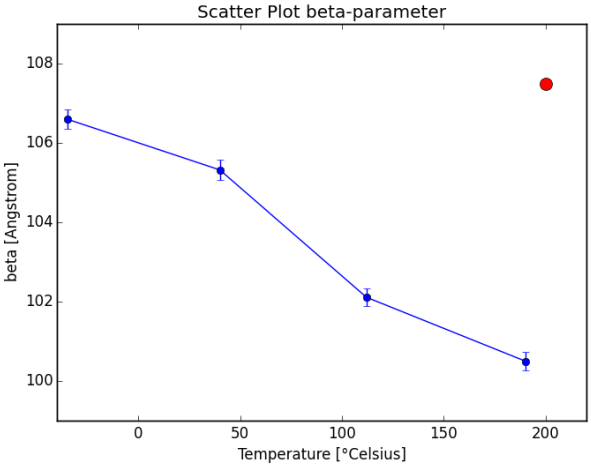

(e) Parameter β

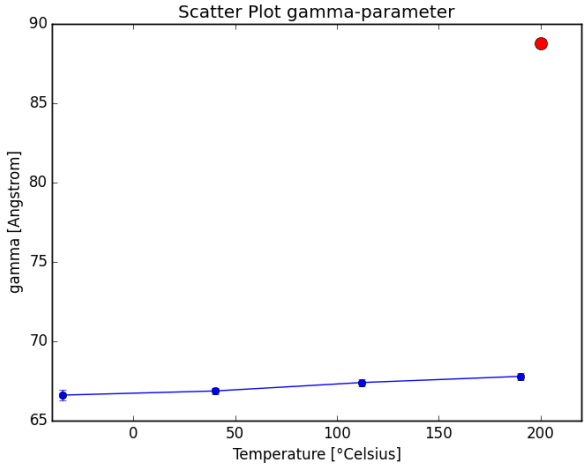

(f) Parameter γ

Figure 3.20: Scatter plots showing the variation of the unit cell parameters of the two different crystal phases of PTCDI-C_8 (blue for ($T = -35$℃ $\div$ $T = 190$℃), red for $T = 200$℃).

Chapter 4

Conclusions

In this study on the PTCDI-C_8 unit cell modifications with temperature has been performed. After having prepared the 2D-powder samples through organic molecular beam deposition, measurements have been performed with synchrotron X-ray beam. A structural investigation of PTCDI-C_8 thin film on SiO_2 was carried out, including the determination of the unit cell parameters and unit cell volume. With the use of X-ray reflectivity it has been possible to check the morphology of the film. As expected, PTCDI-C_8 has grown in high-quality smooth fashion preserving its crystallinity even on the silicon dioxide amorphous substrate. From grazing incidence X-ray diffraction it has been possible to study the thin film crystal structure, analyzing the behaviour of the unit cell while changing the temperature. The unit cell modifications have been studied, leading to positive thermal expansion for b, c, γ unit cell parameters and negative thermal expansion for the a, α, β. For example, it has been shown that the α-angle changed from $\beta \simeq 106.60^\circ$ at $T = -35$℃ to $\beta \simeq 100.50^\circ$ at $T = 190$℃. Moreover, reaching a higher temperature ($T = 200$℃), it has been shown that the GIXD pattern corresponds to a different crystal phase of the PTCDI-C_8 thin film. Analyzing the values of the unit cell parameters they result bigger and out of the previously seen trend. The consequence is an almost doubled unit cell volume, from $V_{unitcell} \simeq 876.56$ ^{3} at $T = 190$℃ to $V_{unitcell} \simeq 1855.33$ ^{3} at $T = 200$℃. reflecting four PTCDI-C_8 molecules per unit cell, almost upstanding. Although, there are still some open questions. One first development should be the determination of the molecular orientation within the unit cell for all the temperatures. Then, a more accurate study on the high temperature crystal phase would be interesting, exploring if there is a

change also in the charge carrier mobility and in the electronic and opto-electronic properties. Then, another step would be to extend this study also to other substituted perylene molecules.

List of Figures

List of Tables

Bibliography

[1] Chihaya Adachi Wolfgang Brütting. *Physics of Organic Semiconductors, 2nd, Completely New Revised Edition*. 2nd ed. Wiley-VCH, 2012. ISBN: 978-3-527-41053-8.

[2] Stephen R. Forrest. "The path to ubiquitous and low-cost organic electronic appliances on plastic." In: *Nature* 428.2 (2004).

[3] Markus Schwoerer and Hans Christoph Wolf. DOI: 10.1002/9783527618651.

[4] Hagen Klauk. *Organic Electronics: Materials, Manufacturing, and Applications*. Wiley-VCH, 2006. ISBN: 978-3-527-31264-1.

[5] Liu Shuhong et al. "Controlled Deposition of Crystalline Organic Semiconductors for Field-Effect-Transistor Applications". In: *Advanced Materials* (2009).

[6] Katz. "Recent Advances in Semiconductor Performance and Printing Processes for Organic Transistor-Based Electronics". In: *Chemistry of Materials* 16.23 (2004). DOI: 10.1021/cm049781j.

[7] *Organic electronics Wikipedia*. https://en.wikipedia.org/wiki/Organic_electronics. Accessed: 2018-05-30.

[8] *Organic photovoltaic advantages.. or challenges? Mapping Ignorance*. https://mappingignorance.org/2016/10/14/organic-photovoltaic-advantages-challenges/. Accessed: 2018-05-30.

[9] Egidius Rutatizibwa Rwenyagila. "Review Article: A Review of Organic Photovoltaic Energy Source and Its". In: 2017 (2017). DOI: 10.1155/2017/1656512.

[10] Zhenan Bao, Jason Locklin, and Gilles Horowitz. "Organic field-effect transistors". In: *CRC Press* 10.5 (2007). DOI: 10.1002/(SICI)1521-4095(199803)10:5<365::AID-ADMA365>3.0.CO;2-U.

[11] Joy C. Perkinson. "Organic field-effect transistors". In: *Opto-Electronics Review* 18.2 (2010). DOI: 10.2478/s11772.

[12] Henning Sirringhaus. "25th anniversary article: Organic field-effect transistors: The path beyond amorphous silicon". In: *Advanced Materials* 26.9 (2014). DOI: 10.1002/adma.201304346.

[13] Joseph Shinar and Ruth Shinar. "Organic light-emitting devices (OLEDs) and OLED-based chemical and biological sensors: An overview". In: *Journal of Physics D: Applied Physics* 41.13 (2008). DOI: 10.1088/0022-3727/41/13/133001.

[14] N. Thejo Kalyani and S. J. Dhoble. "Organic light emitting diodes: Energy saving lighting technology - A review". In: *Renewable and Sustainable Energy Reviews* 16.5 (2012). DOI: 10.1016/j.rser.2012.02.021.

[15] Wolfgang Brütting et al. "Device efficiency of organic light-emitting diodes: Progress by improved light outcoupling". In: *Physica Status Solidi (A) Applications and Materials Science* 210.1 (2013). DOI: 10.1002/pssa.201228320.

[16] Ulrich Hörmann et al. "V_{oc} from a Morphology Point of View: the Influence of Molecular Orientation on the Open Circuit Voltage of Organic Planar Heterojunction Solar Cells". In: *The Journal of Physical Chemistry C* 118.46 (2014). DOI: 10.1021/jp506180k.

[17] Holmes Rysz Opitz Campoy-Quiles Wang Barr Kilcoyne Zhou Dastoor Moons Hansson Ericsson. "Vertical and lateral morphology effects on solar cell performance for a thiophene-quinoxaline copolymer:PC70BM blend". In: *Journal of Material Chemistry A* 3 (2015). DOI: 10.1039/C5TA00683J.

[18] Abhishek P. Kulkarni and Samson A. Jenekhe. "Blue light-emitting diodes with good spectral stability based on blends of poly(9,9-dioctylfluorene): Interplay between morphology, photophysics, and device performance". In: *Macromolecules* 36.14 (2003). DOI: 10.1021/ma0344700.

[19] *Sp2 hybridization - σ- and π-bond.* https://jahschem.wikispaces.com/bonding.

[20] Christopher A. Hunter and Jeremy K.M. Sanders. "The Nature of π-π Interactions". In: *Journal of the American Chemical Society* 112.14 (1990). DOI: 10.1021/ja00170a016.

[21] N. Karl. "Charge-Carrier Mobility in Organic Crystals". In: *Organic Electronic Materials: Conjugated Polymers and Low Molecular Weight Organic Solids*. Ed. by R. Farchioni and G. Grosso. Berlin, Heidelberg: Springer Berlin Heidelberg, 2001. ISBN: 978-3-642-56425-3. DOI: 10.1007/978-3-642-56425-3_8.

[22] Borissov Kiryukhin Rogers Gershenson Podzorov Menard. "Intrinsic Charge Transport on the Surface of Organic Semiconductors". In: *Phys. Rev. Lett.* 93 (2004). DOI: 10.1103/PhysRevLett.93.086602.

[23] Pithan Linus. "Structure, optical properties and light-controlled molecular self- assembly of organic thin films." MA thesis. Berlin: Technische Universität Berlin, 2013.

[24] *Electron mobility Wikipedia*. https://en.wikipedia.org/wiki/Electron$_m$*obility*. Accessed: 2018-07-06.

[25] Tobias N Krauss et al. "Three-dimensional molecular packing of thin organic films of PTCDI-C8 determined by surface X-ray diffraction." In: *Langmuir : the ACS journal of surfaces and colloids* 24 (2008). DOI: 10.1021/la8030182.

[26] Johnson Kloc Siegrist Li-Lin Katz Lovinger and Dodabalapur. In: ().

[27] D. Marcy M. H. Lu T. R. Hebner C. C. Wu and J. C. Sturm. "Ink-jet printing of doped polymers for organic light emitting devices". In: *Applied Physics Letters* 72 (1998).

[28] Charles E. Swenberg Martin Pope. *Electronic Processes in Organic Crystals and Polymers*. 2nd ed. Oxford University Press, 1999. ISBN: 9780195129632.

[29] Anthony. "The Larger Acenes: Versatile Organic Semiconductors". In: *Angewandte Chemie International Edition* 47.3 (). DOI: 10.1002/anie.200604045.

[30] Christos D Dimitrakopoulos and Patrick R L Malenfant. "Organic thin film transistors for large area electronics". In: *Adv. Mater.* 14.2 (2002). ISSN: 0935-9648. DOI: 10.1002/1521-4095(20020116)14.

[31] Shuhei Tatemichi et al. "High mobility n-type thin-film transistors based on N,N-ditridecyl perylene diimide with thermal treatments". In: *Applied Physics Letters* 89.11 (2006). DOI: 10.1063/1.2349290.

[32] C. Rolin et al. “High mobility electron-conducting thin-film transistors by organic vapor phase deposition”. In: *Applied Physics Letters* 93.3 (2008). DOI: 10.1063/1.2958229.

[33] Gelorme Kosbar Graham Curioni Malenfant Dimitrakopoulos and Andreoni. “N-type organic thin-film transistor with high field-effect mobility based on a N,N-dialkyl-3,4,9,10-perylene tetracarboxylic diimide derivative”. In: *Applied Physics Letters* 80.14 (2002). DOI: 10.1063/1.1467706.

[34] Blanco Huang Facchetti Marks Zheng Ortiz Herrera and Segura. “Organic n-channel field-effect transistors based on arylenediimide-thiophene derivatives”. In: *Journal of the American Chemical Society* 132.24 (2010). DOI: 10.1021/ja1018783.

[35] Alejandro L. Briseno et al. “Perylenediimide nanowires and their use in fabricating field-effect transistors and complementary inverters”. In: *Nano Letters* 7.9 (2007). DOI: 10.1021/nl071495u.

[36] J. C. Hwang T. H. Chang L. K. Mao J. Y. Gan and Y. L. Chueh. “The role of water in the device performance of n-type PTCDI-C8 organic field-effect transistors with solution-based gelatin dielectric”. In: *Organic Electronics* 15.4 (2014). DOI: https://doi.org/10.1016/j.orgel.2014.01.023.

[37] Erman Erdoğan and Bayram Gündüz. “Fundamental properties of PTCDI-C8 semiconductor for optoelectronic and photonic applications”. In: *AIP Conference Proceedings* 1815.February (2017). ISSN: 15517616. DOI: 10.1063/1.4976381.

[38] Segger. “Perylene diimide thin films”. MA thesis. Aachen University.

[39] M. Murugavelu et al. “Self-assembly and photophysical properties of a minuscule tailed perylene bisimide”. In: *Materials Science in Semiconductor Processing* 16.2 (2013). DOI: https://doi.org/10.1016/j.mssp.2012.08.001.

[40] L. Bogula. “A novel strategy for enhancing layer-by-layer growth of organic thin films : Temperature variation during individual monolayer growth.” MA thesis. Berlin: Technische Universität Berlin, 2016.

[41] Tobias N. Krauss et al. "X-ray/Atomic Force Microscopy Study of the Temperature-Dependent Multilayer Structure of PTCDI-C8 Films on SiO2". In: *The Journal of Physical Chemistry C* 113.11 (2009). DOI: 10.1021/jp808037w.

[42] M. Yoosuf Ameen et al. "Linearly polarized emission from PTCDI-C8 one-dimensional microstructures". In: *Organic Electronics* 14.2 (2013). DOI: https://doi.org/10.1016/j.orgel.2012.12.012.

[43] *Extreme Brilliant Source project ESRF website*. http://www.esrf.eu/cms/live/live/en/sites/www/home/UsersAndScience/Accelerators/ebs—extremely-brilliant-source.html.

[44] *Synchrotron science - ESRF website*. http://www.esrf.eu/about/synchrotron-science/synchrotron. Accessed: 2018-05-31.

[45] W. Eberhardt. "Synchrotron radiation: A continuing revolution in X-ray science—Diffraction limited storage rings and beyond". In: *Journal of Electron Spectroscopy and Related Phenomena* 200 (2015). DOI: https://doi.org/10.1016/j.elspec.2015.06.009.

[46] R. Feidenhans'l. "Surface structure determination by X-ray diffraction". In: ().

[47] O. Balmes et al. "The ID03 surface diffraction beamline for in-situ and real-time X-ray investigations of catalytic reactions at surfaces". In: *Catalysis Today* 145.3 (2009). DOI: https://doi.org/10.1016/j.cattod.2009.02.008.

[48] *ID03 - Surface Diffraction Beamline ESRF website*. http://www.esrf.eu/UsersAndScience/Experiments/CBS/ID03. Accessed: 2018-05-12.

[49] Harold D. Bale and Paul W. Schmidt. "Small-Angle X-Ray-Scattering Investigation of Submicroscopic Porosity with Fractal Properties". In: *Phys. Rev. Lett.* 53 (6 1984). DOI: 10.1103/PhysRevLett.53.596.

[50] In: ().

[51] L. G. Parratt. "Surface Studies of Solids by Total Reflection of X-Rays". In: *Phys. Rev.* 95 (2 1954). DOI: 10.1103/PhysRev.95.359.

[52] Linus Pithan. “On the Role of External Stimuli to Tailor Growth of Organic Thin Films”. PhD thesis. 2017.

[53] S Kowarik, A Gerlach, and F Schreiber. “Organic molecular beam deposition : fundamentals , growth dynamics , and in situ studies”. In: *Journal of Physics: Condensed Matter* ().

[54] Narang Rahimi and Korakakis. “Optical and morphological studies of thermally evaporated PTCDI-C8 thin films for organic solar cell applications”. In: *International Journal of Photoenergy* 2013.111 (2013).

[55] J.N Hay, J.I Langford, and J.R Lloyd. “Variation in unit cell parameters of aromatic polymers with crystallization temperature”. In: *Polymer* 30.3 (1989). DOI: https://doi.org/10.1016/0032-3861(89)90019-0.

[56] N. T. Wakelyn. “Variation of unit cell parameters of poly(arylene ether ether ketone) film with annealing temperature”. In: *Journal of Polymer Science Part C: Polymer Letters* (1987).

[57] Des McMorrow Jens Als-Nielsen. *Elements of Modern X-ray Physics, 2nd Edition*. Wiley-VCH, 2011. ISBN: ISBN: 978-0-470-97394-3.

[58] Conterio Dove Evans Keen Peters Goodwin Calleja and Tucker. “Colossal Positive and Negative Thermal Expansion in the Framework Material Ag3[Co(CN)6]”. In: *Science* ().

[59] Juhas Billinge Sutton Wilde Bridges Keiber and Kowach. “Local Vibrations and Negative Thermal Expansion in ZrW_2O_8”. In: *Phys. Rev. Lett.* 112 (4 2014). DOI: 10.1103/PhysRevLett.112.045505.

[60] Jacobs Das and Barbour. “Exceptionally large positive and negative anisotropic thermal expansion of an organic crystalline material.” In: *Nature Materials* 9 (2009).

[61] S. Haas et al. “Large uniaxial negative thermal expansion in pentacene due to steric hindrance”. In: *Phys. Rev. B* 76 (20 2007). DOI: 10.1103/PhysRevB.76.205203.

[62] Tobias N Krauss. “Directed Self-Assembly of Organic Semiconductors in Different Dimensionalities.” MA thesis. Stuttgart: Institut für Theoretische und Angewandte Physik der Universität Stuttgart, 2009.

Ringraziamenti

Prima di tutto ci tengo a ringraziare il Prof. Giacomo Ghiringhelli per avermi dato la possibilità di poter lavorare a questa tesi in un grande centro di ricerca quale ESRF.

Then, I want to thank Linus Pithan who has been the best supervisor that I could have ever asked for. Thank you for you time and patience.

I also want to thank all the ID-03 beamline staff: Francesco, Helena, Thomas, Martina, Raja, Maciej and Tommaso. Thank you for welcoming me in your group, it has been a pleasure for me to work with all of you. And thank again to Linus and Martina for your availability in reviewing this thesis.

Vorrei ringraziare tutta la grande famiglia di amici che in questi anni milanesi mi ha fatta sentire a casa e mi ha aiutata a crescere. Alle mie colonne d'Ercole Alessandro *il General* e Andrea *Barbi*. Grazie al mio Giulio *Candre*. Grazie ai miei compagni di avventure Alessandro *AleGi* e Kaveh. Grazie anche agli amici di automazione Franceso, Riccardo e Angelo*ne*. Grazie a Caterina e Filippo e a tutti gli amici di Grenoble. E grazie anche a Marina e Maddalena per gli splendidi momenti passati insieme.
Ringrazio le mie amiche Geraldina e Diana per avermi sopportata e supportata ogni giorno e per essere sempre presenti.
Ringrazio di cuore la mia amica Delfina che nonostante la distanza è sempre stata con me e mi ha sempre sostenuta, e Giacomo, il mio fratello mancato.

Infine, ringrazio la mia famiglia che ha reso tutto questo possibile: mamma Deborah, papà Paolo, nonna Rossella e nonno Giacinto. Ringrazio Tonino e i miei zii Alvaro e Fabiana, Romano, e Sabrina che hanno sempre tifato per me. Ringrazio il mio fidanzato Alberto per aver sempre creduto in me. Un pensiero va alla mia bisnonna Ada a cui avrei tanto voluto raccontare di questa laurea di persona.